ABSTRACT

EVALUATION OF ENVIRONMENTAL MATERIALS AS THERMAL WITNESS MATERIALS

by
Shashank Vummidi Lakshman

New and complex energetic materials are under development for achieving tunable pyrotechnical events for applications such as neutralization of biological weapons, bunker busters and many others. To guide the development of hybrid materials, the pyrotechnical environment they produce requires higher degree of characterization i.e. good description of spatial and temporal temperature distribution.

Temperature measurements in pyrotechnical events are especially challenging, where the temperature of the environment rises more than 2000 K on microseconds to few milliseconds time scale. These environments produce high thermal stress where traditional sensors like thermocouples, optical pyrometers struggle to describe the dynamic changes in the environment.

The presented research focuses on the development of thermal witness materials that are injected into the combustion environment, where they travel with the expanding gases and undergo a quantifiable physical change/transformation. The extent of change is determined post exposure and a correlation is made between the extent of observed change and the exposed time-temperature profile. The thermosensors under investigation, Jarosite and silicate glass are materials that are ubiquitous in both urban and rural environments.

Jarosites undergo decomposition losing (OH) and SO_3 upon thermal exposure. The decomposition mechanism is complex and is governed by a set of serial and parallel

reactions. The degree of decomposition depends on the exposed thermal profile, and can be easily determined using thermogravimetric analysis. A correlation is made between the residual decomposition and the experienced environment. The limitations and sensitivity for these sensors are presented.

The structures of silicate and borate glasses are strongly dependent on the quench rate during glass formation. As an indicator, the glass transition temperature varies linearly with the logarithm of the quench rate. Structural aspects, specifically the degree of connectedness of network forming units [SiO_4] and [BO_3] can be investigated using Raman spectroscopy. This allows one to recognize variations in the temperature, and cooling rate experienced by the material as it cooled from the high-temperature environment. The use of these sensors to reconstruct the environment temperature profile is under development. The fundamental idea defining the methodology to recover thermal history is discussed.

EVALUATION OF ENVIRONMENTAL MATERIALS AS THERMAL WITNESS MATERIALS

by
Shashank Vummidi Lakshman

A Dissertation
Submitted to the Faculty of
New Jersey Institute of Technology
in Partial Fulfillment of the Requirements for the Degree of
Doctor of Philosophy in Chemical Engineering

Otto H. York Department of Chemical, Biological and Pharmaceutical Engineering

August 2014

.

APPROVAL PAGE

EVALUATION OF ENVIRONMENTAL MATERIALS AS THERMAL WITNESS MATERIALS

Shashank Vummidi Lakshman

Dr. Edward L. Dreizin, Dissertation Co-Advisor Date
Professor of Otto H. York Department of Chemical, Biological and Pharmaceutical Engineering, NJIT

Dr. Mirko Schoenitz, Dissertation Co-Advisor Date
Associate Research Professor of Otto H. York Department of Chemical, Biological and Pharmaceutical Engineering, NJIT

Dr. Norman W. Loney, Committee Member Date
Department Chair and Professor of Otto H. York Department of Chemical, Biological and Pharmaceutical Engineering, NJIT

Dr. Robert B. Barat, Committee Member Date
Professor of Otto H. York Department of Chemical, Biological and Pharmaceutical Engineering, NJIT

Dr. Andre Levchenko, Committee Member Date
Applications Scientist, TA Instruments, Princeton Junction, NJ

BIOGRAPHICAL SKETCH

Author: Shashank Vummidi Lakshman

Degree: Doctor of Philosophy

Date: August 2014

Undergraduate and Graduate Education:

- Doctor of Philosophy in Chemical Engineering,
  New Jersey Institute of Technology, Newark, NJ, 2014

- Master of Science in Chemical Engineering,
  New Jersey Institute of Technology, Newark, NJ, 2010

- Bachelor of Engineering in Chemical Engineering,
  Visvesvaraya Technological University, Belgaum, India, 2008

Major: Chemical Engineering

Publications:

Vummidi Lakshman, S., Aly, Y. Schoenitz, M., and Dreizin, E.L. "Characterization of fine Aluminum powder coated with Nickel as a potential fuel additive", Journal of Propulsion and Power, 26 (3) pp. 454-460 (2010).

Vummidi Lakshman, S., Mohan, S., Dreizin, E.L., and Schoenitz, M. "Kinetics of thermal decomposition of a synthetic K-H3O jarosite analog", Journal of Thermal Analysis and Calorimetry 115 (1) pp. 609-620 (2014).

Vummidi Lakshman, S., Dreizin, E.L., and Schoenitz, M. "Evaluation of K-H3O jarosite as thermal witness material", Journal of Thermal Analysis and Calorimetry (accepted).

Presentations:

Vummidi Lakshman, S., Dreizin, E.L., and Schoenitz, M. "Using Quenched Glass Particles to Recover Thermal Histories of Pyrotechnical Events", AIChE Annual Meeting, San Francisco, CA, (2013).

Vummidi Lakshman, S., Dreizin, E.L., and Schoenitz, M. “Measuring thermal histories using fragile glass crystallization ", AIChE Annual Meeting, Pittsburg, PA, (2012).

Vummidi Lakshman, S., Dreizin, E.L., and Schoenitz, M. “Irreversible phase transitions for rapid high temperature measurements ", AIAA Region I Young Professional, Student, and Education Conference, Laurel, MD, (2011).

Vummidi Lakshman, S., Dreizin, E.L., and Schoenitz, M. “Irreversible phase transitions for rapid high temperature measurements ", 7th US National Combustion Meeting, Atlanta, GA, (2011).

Vummidi Lakshman, S., Dreizin, E.L., and Schoenitz, M. “Irreversible phase transitions for rapid high temperature measurements ", AIChE Annual Meeting, Salt Lake City, UT, (2010).

Poster Presentations:

Vummidi Lakshman, S., Dreizin, E.L., and Schoenitz, M. “Evaluation of glass materials as thermal witness materials ", Danna Knox Engineering Showcase, Newark, NJ, (2014).

Vummidi Lakshman, S., Dreizin, E.L., and Schoenitz, M. “Evaluation of glass materials as thermal witness materials”, Johnson and Johnson Engineering Showcase, New Brunswick, NJ, (2014).

Vummidi Lakshman, S., Dreizin, E.L., and Schoenitz, M. “Evaluation of glass materials as thermal witness materials”, AIChE Annual Meeting, San Francisco, CA, (2013).

Vummidi Lakshman, S., Dreizin, E.L., and Schoenitz, M. “Evaluation of glass materials as thermal witness materials”, Annual Graduate Student Research Day NJIT, Newark, NJ, (2013).

Vummidi Lakshman, S., Dreizin, E.L., and Schoenitz, M. “Recovering thermal histories from quenched glass”, DTRA Basic Research Technical Review, Springfield, VA, (2013).

Vummidi Lakshman, S., Dreizin, E.L., and Schoenitz, M. “Measuring thermal histories using fragile glass crystallization”, Annual Graduate Student Research Day NJIT, Newark, NJ, (2012).

Vummidi Lakshman, S., Dreizin, E.L., and Schoenitz, M. “Validation of the use of jarosite thermal decomposition as a method to record thermal histories”, DTRA Basic Research Technical Review, Springfield, VA, (2012).

Vummidi Lakshman, S., Dreizin, E.L., and Schoenitz, M. “Validation of the use of jarosite thermal decomposition as a method to record thermal histories”, Gordon Research Conference (Energetic Materials), West Dover, VT, (2012).

Vummidi Lakshman, S., Dreizin, E.L., and Schoenitz, M. “Measuring thermal histories using jarosite particle decomposition”, Annual Graduate Student Research Day NJIT, Newark, NJ, (2011).

Vummidi Lakshman, S., Dreizin, E.L., and Schoenitz, M. “Validation of the use of jarosite thermal decomposition as a method to record thermal histories”, DTRA Basic Research Technical Review, Springfield, VA, (2011).

Vummidi Lakshman, S., Dreizin, E.L., and Schoenitz, M. “Measuring thermal histories using jarosite particle decomposition”, Annual Graduate Student Research Day NJIT, Newark, NJ, (2010).

I dedicate my PhD thesis to my wonderful parents Shantha Vummidi Lakshman and Vummidi Lakshman for their love, wisdom, guidance and immense encouragement throughout my journey.

A message from the true optimist in me:
"It is difficult to say what is impossible, for the dream of yesterday is the hope of today and the reality of tomorrow." - Robert H. Goddard

ACKNOWLEDGMENT

I would first like to acknowledge my advisors, Dr. Edward Dreizin and Dr. Mirko Schoenitz because without their guidance and support, this work would not have been possible.

I offer my heartfelt gratitude to Dr. Mirko Schoenitz for being an instrumental influence in my journey at NJIT. I appreciate all the time and valuable input he has provided me throughout the years. My skills as a researcher was developed based on his approach to deduce and discretize problems. My ability to perceive information and my confidence in expressing and communicating has grown tremendously through his influence. His mentorship and trust in me has allowed me to get exposed to various research tools and analysis processes. His patience and intellect has helped me in completing a challenging dissertation topic. It was a pleasure being mentored by him.

I offer my deepest gratitude to Dr. Edward L. Dreizin for providing a stable and a constant source of encouragement, inspiration and optimism during the pursuit of my degree at NJIT. I joined Dr. Dreizin's group as a master's student and was thoroughly inspired by his method of mentorship and dedication he showed towards the development of my skill both professional and personal. His ability to develop and maintain a nurturing research environment was paramount in my decision of pursuing a PhD degree. My presentation and communication skills were developed by his encouragement to participate and present at several conferences and competitions each year. He has helped me to be more rounded and an optimistic person. It was a pleasure working with him, and I could not have asked for a better advisor.

I would also like to thank the other members of my dissertation committee, Dr. Andre Levchenko, Dr. Norman W. Loney and Dr. Robert B. Barat, for their thoughtful criticism and their much appreciated feedback.

I would like to express my gratitude to Vern Hoffmann for his assistance and guidance during the years. I appreciate his wisdom in constructing laboratory experiments and machining various components. I have learnt a great deal from him, and I feel privileged to have worked with him. I would like to express my appreciation to Dr. Alexandre Ermoline, Dr. Salil Mohan and Dr. Robert Gill in their assistance over the years.

I must acknowledge my fellow students for all their support and assistance. Many thanks to Demitrios Stamatis, Ervin Beloni, Priya Santhanam, Yasmine Aly, Shasha Zhang, Carlo Badiola, Rayon Williams, Hongqi Nie, Amy Corcoran, Ani Abraham, Ian Monk and Song Wang .

I owe my parents, Shantha Vummidi Lakshman and Lakshman Vummidi a debt of gratitude, their constant encouragements and support has fueled my ambitions and confidence in pursuing my career. I would like to thank my family and friends for their moral and support.

Finally, I acknowledge our sponsors, Defense Threat Reduction Agency (DTRA), for the financial support.

TABLE OF CONTENTS

TABLE OF CONTENTS
(Continued)

TABLE OF CONTENTS
(Continued)

LIST OF TABLES

LIST OF FIGURES

LIST OF FIGURES
(Continued)

LIST OF FIGURES
(Continued)

CHAPTER 1

INTRODUCTION

1.1 Background

In recent years significant effort has been focused on tools and methods suitable for destroying biological weapon stockpiles. Typical methods, such as use of high powered ordnances aimed at incinerating these materials have poor neutralization efficiency. The studies conducted by Nelson et al. [1] indicate that the use of "bunker-busters" causes aerosolization of the viable biological agent particles that results in collateral damage. Alternate methods to neutralize biological agents that could have escaped from the high-temperature/high pressure zone produced in a blast have gained popularity. Since there is a wide range of biological agents, a broad-spectrum of biocidal materials was considered as additives to new hybrid energetic materials employed in advanced munitions [1]. Explosions generated by these munitions produce short-lived, high-temperature dynamic environments. Advanced energetic formulations and designs of explosive charges enable one to vary spatial and temporal temperature distributions inside the generated fire balls, which may need to be optimized to take full advantage of specific biocidal additives used and maximize inactivation of aerosolized biological agent particles. Quantitative measurements of temperature distributions in dynamic environments generated by the fire balls are necessary to validate, optimize, and improve the state of the art hybrid energetic systems and components.

Pyrotechnical events occur with a sudden release of immense energy producing a spike in the temperature and pressure of the surrounding environment. During a typical pyrotechnical event, temperatures can rise above 2000 K for durations of milliseconds to

seconds. Nevertheless, the interiors of combustion clouds are not easily accessible for temperature measurements. Direct temperature measurements for these events are extremely challenging. Traditional temperature measurement devices like thermocouples and other electronic devices are either slow, or prone to failure due to the high stress environment created by these events. Typical combustion clouds are laden with incandescent particles resulting in optically thick environments; hence optical techniques can measure only the expanding outer layer of the combustion event. Efforts have been made to use spectroscopic techniques such as Coherent Anti-Stokes Raman Spectroscopy (CARS) and Fourier Transform Infrared Spectroscopy (FT-IR) to provide a real time temperature measurement by investigating the spectroscopic signatures of the reactive species. These techniques always provide a line of sight average and also prone to interference from other debris in the expanding combustion environment.

1.2 Objective

Current research is motivated by the development of novel methods to measure temperature-time distributions in a fireball. Since traditional techniques are inadequate and since the main objective is to describe the effect of environment on biological agents; particle-based thermal witness materials are favorable. Materials exposed to a high-temperature environment will generally change over the duration of the exposure, be it due to irreversible phase changes, or due to other time-dependent processes such as heat and mass transfer. However, after the exposure, only an integral effect is observed in each particle. The most challenging requirement for particulate witness materials in short-lived high-temperature environments is therefore to develop an approach by which time and temperature effects can be decoupled. That is, it is required to be able to

distinguish a witness material that was exposed to high temperatures for a short time from one that was exposed to a relatively lower temperature for a longer time even though the total energy absorbed by the material may be the same. An additional requirement based on the context of biological agent defeat applications is to mimic the effect of environment on biological agents, namely bacterial spores. These particle sensors are preferred to be of similar size, densities and show properties representing biological agents. Apart from that these sensors need to be able to survive the high-stress events, and to be recovered reliably post-exposure.

The approach developed in the present research focuses on two potential thermal witness materials. The first is a complex sulfate hydrate which undergoes irreversible thermal decomposition upon heating. A detailed decomposition mechanism describing all individual reactions occurring during decomposition is developed. The ability of this mechanism to help recover thermal exposure conditions is tested. The second is a silicate glass, which by the dependence of the glass transition on the cooling rate allows the reconstruction of partial, but practically relevant temperature-time histories. Part of the analysis is a heat transfer model based on the thermophysical properties of the sensors. With a certain degree of limitation, the pyrotechnical event can be described in its entirety by a combination of the developed thermosensors and complementing exposure recovery procedure. Use of thermosensors of different sizes, which would exhibit different material evolution upon exposure to the same dynamically changing temperature profile, will help decoupling the effect of time and temperature of the exposure.

CHAPTER 2

KINETICS OF THERMAL DECOMPOSITION OF A SYNTHETIC K-H_3O JAROSITE ANALOG

2.1 Introduction

Jarosites are complex sulfate hydrates that belong to the alunite super group. Potassium jarosite with the formula $KFe_3(SO_4)_2(OH)_6$ is a common mineral found in weathering zones of sulfide ore deposits and a common byproduct of mining operations [2, 3]. The material is relevant to many industrial processes [2, 4], and it has received recent interest as a hydrous mineral on the surface of Mars, possibly indicating the past presence of liquid water [5-7].

The thermal decomposition of K-jarosite and other members of the jarosite and alunite groups have been studied previously. A number of reaction sequences describing the decomposition have been proposed [8, 9], and the structural implications of jarosite decompositions have been published by [10]. The decomposition occurs as a series of well-distinguished steps, where adsorbed water, $(OH)^-$ groups, and $(SO_4)^{2-}$ groups are lost sequentially. Jarosite in the strict sense ceases to exist after the loss of $(OH)^-$ groups. However, it was attempted to establish a comprehensive model covering the loss of the $(SO_4)^{2-}$ groups as well. No comprehensive kinetic study of the thermal decomposition has been published so far.

The present study attempts to develop a comprehensive kinetic model for the thermal decomposition of potassium jarosite. The motivation for this research derives from a need for thermal witness materials [11-13]. It is desired to identify materials that give unique phase compositions when they are exposed to complex and rapidly changing thermal conditions, such as occurring in a fire or explosion. Background to this are

investigations on how biological agents such as exist in bio-weapon stockpiles react to thermal stresses in combustion events. It should be possible to readily determine the extent of partial decomposition after such exposure, and it should also be possible to relate the extent of partial decomposition to the temperature-time histories experienced by the material. In a realistic situation such a thermal history would likely not be completely unknown, but could be modeled subject to a number of unknown parameters and boundary conditions. Even if a witness material could not recover the complete thermal history with high fidelity, it may give enough information to aid hydrocode modeling efforts [14].

Jarosite is of interest because it decomposes in multiple steps that are well resolved, at least under thermal analysis conditions [8, 9, 15]. If the decomposition rates for the individual steps are sufficiently distinct, then it should be possible in principle to correlate the phase makeup of partially decomposed jarosite with the thermal history that caused the partial decomposition. Interrogation of partially decomposed jarosite, that is, determining the extent of partial decomposition, should be readily possible by conventional thermoanalytical methods. However, all these considerations presuppose a reliable kinetic model of the decomposition that is valid over a wide range of temperatures and on a wide range of time scales. This work is focused on the development of such an experimentally validated model.

The use of materials with complex decomposition behavior, such as jarosites, as thermal witness materials imposes a number of constraints, especially on particle size. The intended application would disperse the witness particles in a high-temperature gaseous environment so that the individual particles follow the same trajectories and

experience the same temperature-time histories as everything else in the combustion environment, specifically the biological agents of interest. This means that there should be no significant particle settling over time periods of seconds, and there also should not be significant thermal gradients, or heat-up times. This effectively means that the particle size should be on the order of 10 μm or less, and the present work focuses on such particles.

A corresponding manuscript addressing validation of the thermal decomposition model developed here is in preparation. Aside from the specific application motivating this study, developing a decomposition model may benefit investigations of the evolution of Mars and its atmosphere (see [6] and references therein).

2.2 Experimental Setup

2.2.1 Synthesis

In order to help thorough characterization, the present study used synthetic material instead of a natural jarosite. For simplicity and in keeping with common practice we will refer to this material simply as (K,H_3O) jarosite for the remainder of the manuscript. Jarosite was synthesized according to the methodology published by [16-18]. A solution of 4.41 g of potassium sulfate (K_2SO_4, Alfa-Aesar, 99.0%) and 20.0 g of iron sulfate ($Fe_2(SO_4)_3$, Alfa-Aesar, reagent grade) in 150 mL water was refluxed for seven days in a silicone oil bath. The molar ratio of potassium to iron in the initial charge was set to 2 and the pH was between 0-1. The jarosite precipitated from the solution was filtered out. It was initially dried at 65 °C for 18 hours under vacuum. The actual yield of particulate jarosite was 15.7 g, or 62 % of the theoretical maximum yield. This is in general

agreement with the references for the synthesis method. Substantial amounts of the product adhered to the synthesis vessel, but were not recovered as the prepared amounts were considered sufficient for the present purposes.

In a subsequent step, the particle size was modified by rolling the jarosite powder as water-based slurry for 9 hours in a horizontal roller mill using 3/16" diameter zirconia balls as milling media. This reduced the initial wide size distribution to give a narrow distribution with a volume-average below 10 μm in accordance with particle size requirements outlined in the introduction above. The milled jarosite was dried at 100 °C for 18 hours under a mild vacuum.

2.2.2 Characterization

SEM images were taken using a Phenom Tabletop Microscope by FEI Technologies, Inc. Particle size distributions were measured using a Beckman Coulter LS230 Enhanced Particle Analyzer. For the size analysis, the particles were prepared in a water-based suspension. A Mie scattering model was used, with the real and imaginary components of the complex refractive index of jarosite set to 1.815 and 0, respectively [19].

X-ray diffraction (XRD) patterns were collected using a Philips X'pert MRD powder diffractometer operated at 45 kV and 40 mA and using unfiltered Cu K_α radiation (average λ = 1.5418 Å). The x-ray patterns were collected with a step size of 0.03 ° 2Θ. The pattern of the as-synthesized material was further subjected to whole pattern refinement using GSAS software (General Structure Analysis System, [20]) to obtain compositional information.

2.2.3 Thermal Analysis

Thermo-gravimetric analysis (TG) was performed using a TA Instruments model Q5000IR thermo-gravimetric analyzer. The balance was purged with argon (Matheson Tri-Gas, 99.999%) at 10 ml/min and the furnace was purged with air (Airgas, zero grade) at 25 ml/min. Alumina pans were used. The instrument was calibrated using the Curie points of alumel, nickel, and cobalt, and the melting points of indium, tin, bismuth, zinc, and aluminum. The calibration was performed at heating rates from 5 to 50 K/min. Since the control software does not allow for calibration at varying heating rates, measurements were performed in calibration mode, and the temperatures were corrected thereafter. Sample masses of ~1 mg were used, and baseline corrections became significant. Therefore, each sample was heated twice without removing the sample from the TG. The actual decomposition was recorded during the first cycle, and the baseline during the second cycle. Decomposition corrected for baseline effects are obtained by the difference of the first and second heating curves. Decomposition was studied at heating rates ranging from 5 to 50 K/min.

In addition to measurements at constant heating rates, measurements were also carried out at constant reaction rates. The actual heating rate was controlled in such a way that the observed mass loss rate was kept constant at respective values between 0.05 and 0.398 %/min.

To verify the decomposition sequence, material was heated in the TG to intermediate temperatures, and partially decomposed material was obtained and analyzed by XRD.

2.3 Results

2.3.1 General Characterization

An overview of the powder is shown in Figure 2.1. The particles are non-spherical with jagged edges, but otherwise equiaxed. Some closed porosity is observed, possibly indicating inclusions of water or synthesis solution.

The size distribution of the processed particles is shown in Figure 2.2 The volume based mean particle diameter is close to 5 μm and a significant fraction of particles are less than 10 μm.

From the synthesis procedure, the jarosite was expected to have potassium and hydronium components. X-ray diffraction was performed to determine the actual composition as well as the phase purity of the material. The diffraction pattern is shown in Figure 2.3.

All observed peaks can be attributed to jarosite, and no crystalline impurities were observed. The lattice parameters were determined by whole-pattern fitting as a_0 = 7.30253(1) Å and c_0 = 17.20561(5) Å with the refinement error in the last digit given in parentheses.

Composition was evaluated using two independent indicators. From the literature it was known that the a_0 and c_0 lattice parameters depend on the K concentration. The following linear dependencies were extracted from ref [21]: $x_K = -17.097 \cdot a_0 + 125.77$ and $x_K = 5.801 \cdot c_0 - 98.90$. From the observed lattice parameters x_K was calculated to be 0.924±0.044 and 0.919±0.043, respectively. Both values are in good agreement. While this result suggests the presence of the corresponding amounts of $(H_3O)^+$ on the K site in the jarosite structure, it has been argued in the literature that there is no strict reason why

the K structural site must be completely occupied [22]. Therefore, the amount of $(H_3O)^+$ can not be regarded as conclusively determined by XRD.

In addition to the compositional variability on the K site, the amount of Fe in the structure can vary [3, 22]. Still, there is no clear dependence of the lattice parameters on the Fe concentration. Therefore, the composition was determined by whole pattern refinement. The jarosite structure data was obtained from the literature [21], and only site occupancies were refined. Results showed the occupancy of the K site by K as 0.927±0.011 in good agreement with the results shown above. The iron site occupancy was determined as 0.987±0.005.

The deficiencies on the positive-ion structural sites must be balanced by incomplete occupancies of negative ion sites. Following convention (e.g., [22]), it was assumed that the sulfur sites are completely occupied, and charge balance is achieved by removing $(OH)^-$ groups. Therefore, the composition of the jarosite used in this study was determined as $(H_3O)_xK_{0.92}Fe_{2.96}(SO_4)_2(OH)_{5.88-y}\cdot zH_2O$ where y denotes the amount of vacancies on the K structural site, and $x + y = 1- 0.92$. This leaves x and y as compositional variables, together with any adsorbed water. All of these are relevant for thermogravimetry, and will be determined from the thermogravimetric measurements.

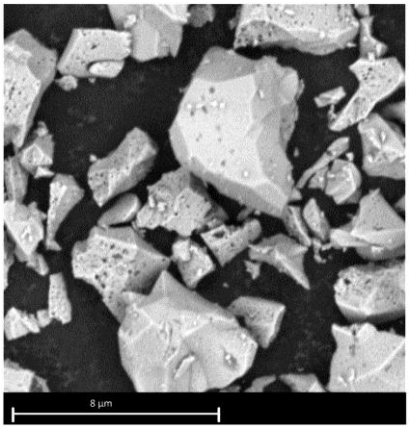

Figure 2.1 Backscattered electron image of jarosite as synthesized.

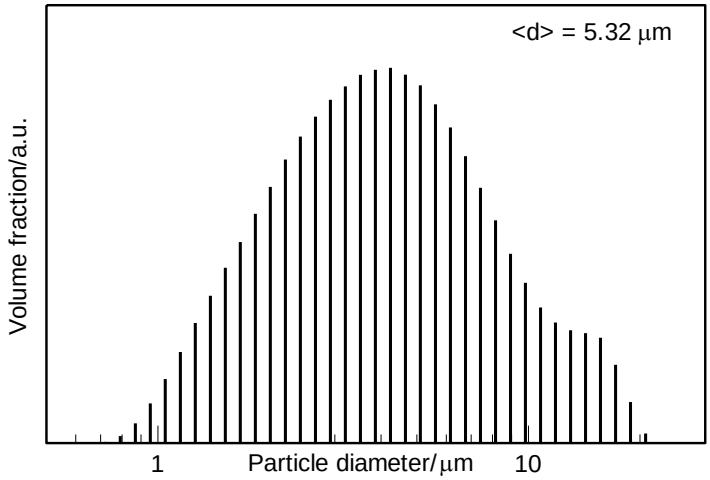

Figure 2.2 Particle size distribution of jarosite after rolling treatment.

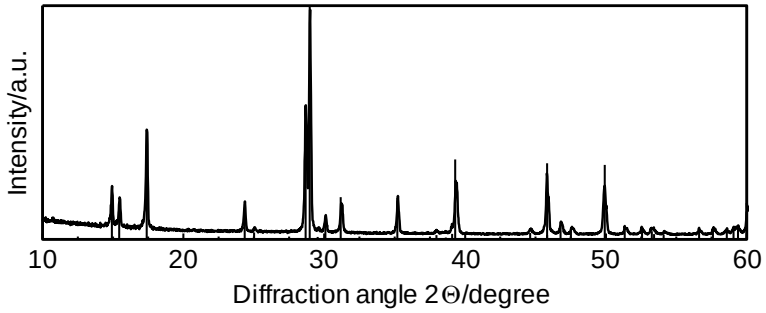

Figure 2.3 X-ray diffraction pattern of K-H_3O jarosite as synthesized.

2.3.2 Thermal Decomposition

Typical decomposition behavior of the untreated material is shown in Figure 2.4. The top curve shows the decomposition at a constant heating rate of 5 K/min. The bottom curve shows decomposition recorded at a constant reaction rate, where the heating rate was continually adjusted to achieve a set mass loss in mg/min. As previously reported, thermal decomposition occurs in several steps [8, 9, 15, 23]. The first stage has been attributed to the loss of adsorbed water, the second stage to the loss of $(OH)^-$ in the form of water and the last stage to the loss of $(SO_4)^{2-}$ groups in the form of SO_3, which may further decompose to SO_2 and O_2. Due to the initial treatment of the jarosite at 100 °C under vacuum, the initial water loss is not distinct in Figure 2.4. The SO_3 loss stage shows some internal structure, suggesting several decomposition reactions. This stage is better resolved in the constant-reaction rate curve (Figure 2.4).

The amount of adsorbed water can only be calculated by comparing the total mass loss against the calculated mass loss. Hydronium and vacancies on the K site may be determined similarly.

Preliminary experiments had showed that the treatment of the material prior to TG analysis had an influence on the resulting curves. Material that was not size-reduced as described above showed a number of well-separated decomposition steps in the $(OH)^-$ loss segment in the 600-700 K range, similar to the behavior reported by Frost et al. [8, 9]. Those steps were not present in the size-reduced material used here. In addition, the amount of material used to conduct the TG experiments affected the observed decomposition behavior. Figure 2.5 shows the derivative of the TG curves as a function of sample mass in the temperature interval where SO_3 is lost. The temperature at which

decomposition was observed, as well as the number of apparent sub-reactions changed. Given the context of this research, smaller masses were chosen for further analysis as a better approximation of single-particle decomposition behavior.

To verify the general decomposition sequence, samples were heated to 528 K, 710 K and 1073 K, and partial decomposition products were recovered at room temperature after allowing the TG to cool, and analyzed. The effective cooling rate varied depending on the temperature, but generally measured in degrees per minute. Since the gaseous decomposition products were effectively removed, back-reactions were not expected to occur. SEM micrographs are shown in Figure 2.6. Particles remain intact; disintegration is not observed. The recovered material was examined by XRD. In addition, material was also recovered from the constant-reaction rate experiment at 839 K. The corresponding XRD patterns are shown in Figure 2.7. The jarosite pattern for the sample recovered from 528 K, after the adsorbed water loss is identical to that of the initial material. Therefore, no structural changes occur due to the loss of adsorbed water. It is likely that this water is loosely bonded to the surface, or resides in the porosity that was observed in Figure 2.1. The only difference between the material recovered from 528 K and the starting material is the appearance of two small peaks near 28 °2Θ, consistent with the onset of formation of $Fe(SO_4)(OH)$. The sample recovered from 710 K, above the OH loss, is largely amorphous. Weak peaks are visible of $Fe(SO_4)(OH)$, $KFe(SO_4)_2$, and of β-Fe_2O_3. The material recovered from the constant-reaction-rate experiment at 839 K is also poorly crystalline, and contains some amount of β-Fe_2O_3 and $K_3Fe(SO_4)_3$ (identified using reference 30-0943, PDF-4+ Database, ICDD 2010). The final

decomposition product, recovered from 1073 K shows only α-Fe_2O_3 and K_2SO_4 as crystalline phases.

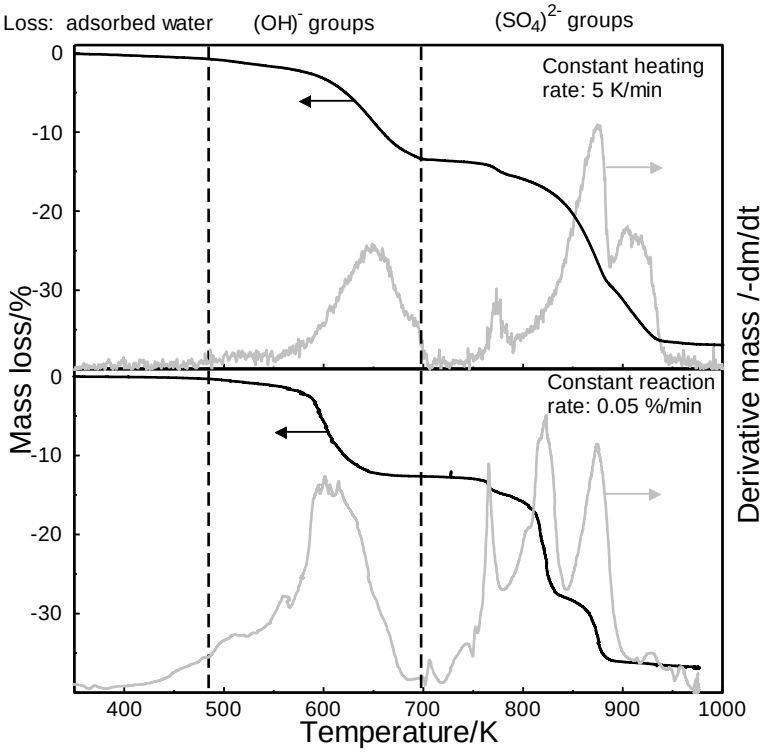

Figure 2.4 Mass loss and derivative mass loss of jarosite heated at 5 K/min and under constant-reaction rate conditions.

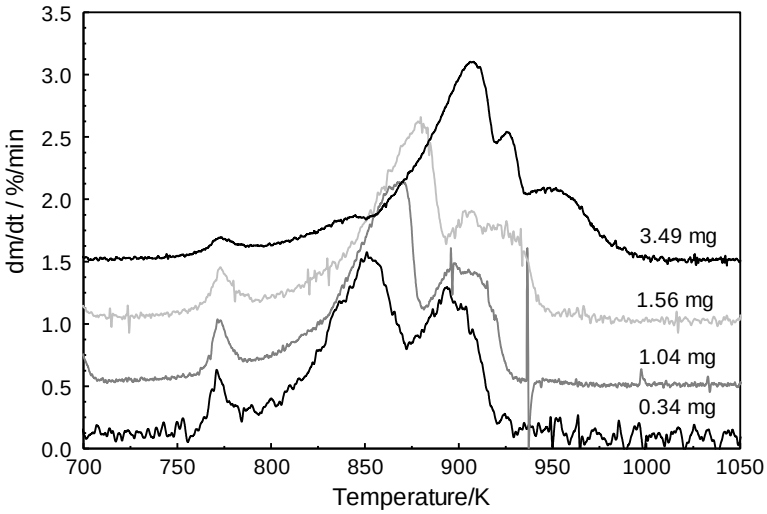

Figure 2.5 Derivative mass loss recorded at 5 K/min with varying sample masses.

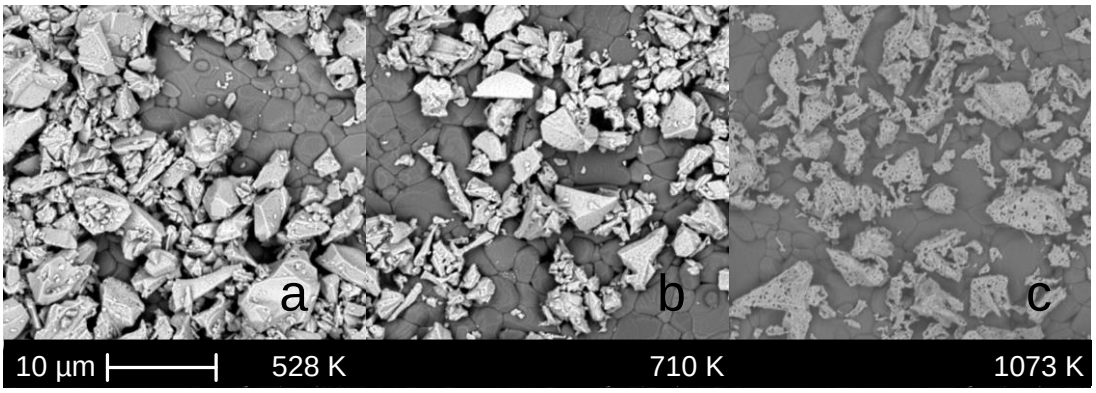

Figure 2.6 Backscattered electron images of partially decomposed jarosite recovered from TG experiments. Samples a, b, and c were recovered after heating to 528, 710, and 1073 K, respectively.

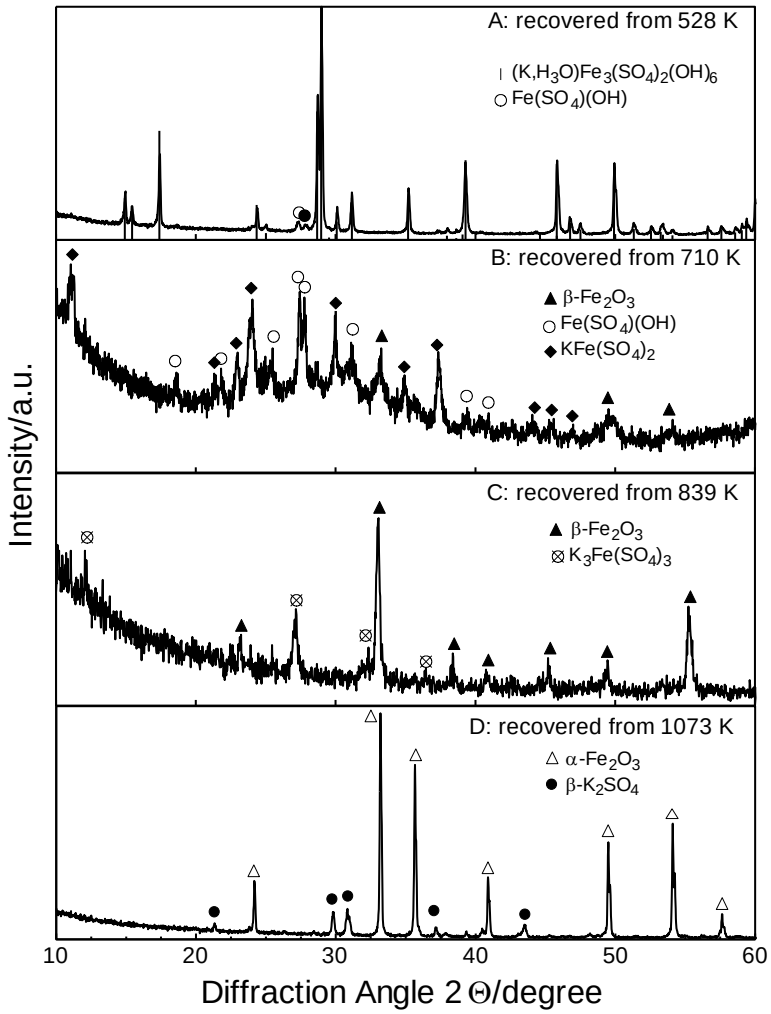

Figure 2.7 XRD patterns of partial decomposition products of K-H3O jarosite recovered from TG experiments.

To determine kinetic relations, measurements over a range of heating rates were performed. As an initial assessment, the apparent activation energy as a function of the sample mass, m, based reaction progress, $\alpha = (m-m_{initial})/(m_{final}-m_{initial})$, was determined by isoconversion analysis [24]. Both measurements at different constant heating rates, and measurements at different constant reaction rates were processed. The results are shown in Figure 2.8. While strictly speaking it should be possible to use all measurements regardless of measurement mode for isoconversion analysis, the results between the two

modes are similar but not entirely identical to each other. Several intervals in α with relatively constant apparent activation energies can be distinguished in either measurement mode. The divergent behavior seen at $\alpha \rightarrow 0$, $\alpha \approx 0.35$, and $\alpha \rightarrow 1$ is an artifact commonly observed in regions were the reaction progress α changes very little as a function of temperature. The range $\alpha = 0.05 - 0.35$, attributed to the loss of $(OH)^-$ shows an average apparent activation energy of 160 kJ/mol under constant heating rate conditions. At the end of this step, near $\alpha = 0.35$, a short interval with a higher activation energy approaching 300 kJ/mol, can be identified in Figure 2.8. The corresponding interval under constant reaction rate conditions shows a higher average activation energy between $\alpha = 0.05$-0.35, around 200 kJ/mol, and the end of the interval at $\alpha = 0.35$ shows an elevated apparent activation energy as well.

After this mass loss step, a small step near 800 K can be identified in Figure 2.4. This step is perhaps even more distinct under constant reaction rate conditions, see Figure 2.4. However, it can not be unambiguously distinguished in either isoconversion result in Figure 2.8.

The following interval $\alpha = 0.45 - 0.75$ shows again a relatively constant average apparent activation energy of 225 kJ/mol with constant heating rate and constant reaction rate measurements in agreement. Under constant heating rate conditions, this interval transitions to a region with an apparent activation energy of 350 kJ/mol around $\alpha = 0.8$, and the decomposition ends with an interval between $\alpha = 0.86 - 0.97$ with an apparent activation energy of 180 kJ/mol. Similar behavior can be seen under constant reaction rate conditions with somewhat different energy values. The apparent activation energy

rises to 285 kJ/mol at α = 0.75, remains constant until α = 0.85, and then gradually returns to about 225 kJ/mol.

While some of the individual reactions can be distinguished, it is clear that not all reactions participating in the decomposition can be identified from Figure 2.8. For the decomposition model developed here, activation energies describing the $(OH)^-$ loss and the main SO_3 loss were taken from the isoconversion analysis, and not further modified. All other activation energies were determined separately, as described below.

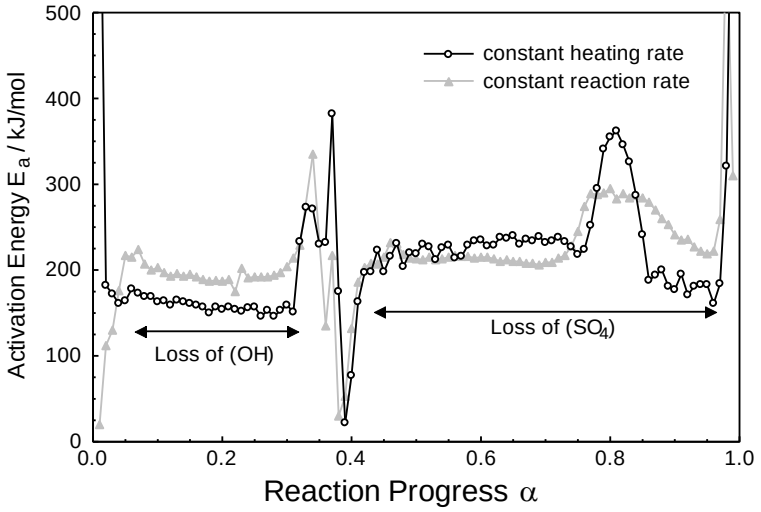

Figure 2.8 Apparent activation energies determined by isoconversion analysis of constant-heating-rate and constant-reaction rate measurements.

2.3.3 Decomposition Model

According to the composition $(H_3O)_xK_{0.92}Fe_{2.96}(SO_4)_2(OH)_{5.88-y}$ determined above, the jarosite can be effectively partitioned in three components: the potassium component $0.92\cdot KFe_{2.96}(SO_4)_2(OH)_{5.88}$, the hydronium component $x\cdot(H_3O)Fe_{2.96}(SO_4)_2(OH)_{5.88}$, and the balance associated with the vacancies on the K site $y\cdot Fe_{2.96}(SO_4)_2(OH)_{4.88}$.

Parameters *x* and *y*, as well as the amount of any adsorbed water, $z{\cdot}H_2O$, (parameter *z*) must be determined from mass balance, and matched to the observed thermogravimetric curves. Since three parameters can not be determined from just one observable, such as the total mass loss, it must be assumed in which respective temperature ranges the individual contributions should occur, and with what major features of the thermogravimetric curves they should be associated.

First, it was assumed that adsorbed water is effectively lost before the onset of SO_3 loss. Non-structural water is not typically stable at temperatures exceeding 500 K in dry air [25].

Second, it was assumed that $(H_3O)^+$ is lost concurrent with the main SO_3 loss feature. Frost et al. [9] investigated the thermal decomposition of hydronium jarosite and reported the loss of the $(H_3O)^+$ constituent at temperatures above the loss of the $(OH)^-$ groups.

Third, the "vacancy component" was assumed to decompose completely in parallel to the other $(OH)^-$ loss reactions. That is, since this component does not correspond to an otherwise identifiable phase, it is assumed that it is completely removed from the material once the associated $(OH)^-$ groups are lost. The vacancy component accounts for a minor fraction of the observed mass loss. No minor aspect of the decomposition curves could be correlated with these amounts of $(OH)^-$ and $(SO_4)^{2-}$, and so the simplest assumption was followed.

With these assumptions, the mass loss was calculated at the end of the decomposition, and at the onset of the SO_3 loss. Adjusting *x*, *y*, and the amount of

adsorbed water, z, to match the observed curves, the parameters were estimated to x = 0.058, y = 0.022, and z = 0.35.

The decomposition model was based on Arrhenius kinetics, where the rate is determined by a temperature factor, $k(T) = A \cdot \exp(-E_A/RT)$, and a factor dependent on the reaction progress, $f(\alpha)$, typically referred to as the reaction model:

$$\frac{d\alpha}{dt} = k(T) \cdot f(\alpha) \tag{2.1}$$

An attempt was made to assign an activation energy, a pre-exponential factor, and a reaction model to each sub-reaction. For this purpose, the reaction progress α was individually defined for each reaction. As an example, the reaction progress describing the loss of adsorbed water was defined as:

$$\alpha_{water} = 1 - n_{water} / z \tag{2.2}$$

where n_{water} is the molar amount of adsorbed water present at any given time, and z is the maximum amount of water contained in the material as defined above. The global reaction progress is calculated as the sum of the individual α values:

$$\alpha = \sum_i \alpha_i M_i / M_{total} = 1 - M / M_{total} \tag{2.3}$$

where the subscript i denotes the individual components, M_i is the molar mass of the individual component, M_{total} is the molar mass of the jarosite according to the

composition determined, and M is the instantaneous molar mass of the decomposing jarosite.

The reaction scheme as given below consists of sequential and parallel reactions. In the case of sequential reactions, the product of the leading reaction is taken as the starting material of the following reaction, so that

$$n_j = 1 - n_i \cdot M_j / M_i \tag{2.4}$$

where n_i and n_j are the molar amounts of the components i and j, respectively. Reaction models were initially assumed to be first-order, $f(\alpha) = 1-\alpha$, so Equation(2.1) transformed to:

$$\frac{d\alpha}{dt} = A \exp\left(-\frac{E_A}{RT}\right) \cdot (1-\alpha) \tag{2.5}$$

Adjustments were made based on how well the calculated mass loss matched the observation. Where possible, activation energies were taken from the isoconversion analysis above (see Figure 2.8), and pre-exponential factors were treated as adjustable parameters.

To perform the actual computation, the relations were implemented in MATLAB software. After initial assignment, the set of reaction Equations were iterated over time, and the molar amounts of all components were tracked. Once the amount of a given component that was present in the initial material was completely depleted, the calculation for that component was terminated. In some rare cases, it is possible that the

amount of a component is zero even though the component is actively being formed. This occurs when the decomposition reaction is faster than the formation reaction. In such cases, the amount of component actually formed during an iteration step was used as the limit for the decomposition reaction.

Specific aspects of the decomposition will be discussed first in order to specify relevant issues. After this introduction, the global scheme for the decomposition will be presented.

2.3.3.1 Adsorbed Water. The loss of adsorbed water appears to have no structural implication, and was therefore assumed to occur at low temperatures, in parallel to all other reactions. The reaction model was found not to have a significant effect on the match between observation and calculation, and was therefore left at first-order. The pre-exponent and activation energy for this reaction were chosen so that this minor effect would not overlap any other reactions. The amount of adsorbed water is so small that no specific conclusions could be drawn from the observed TG curves.

2.3.3.1 $(OH)^-$ Groups. The starting point of $(OH)^-$ decomposition is the undecomposed jarosite, since the adsorbed water loss has no discernible effect on the structure. The final product of the $(OH)^-$ loss in an ideal K-jarosite consists of Fe_2O_3 and $KFe(SO_4)_2$, yavapaiite. In an earlier report, the loss of $(OH)^-$ from jarosites and alunites were divided into individual steps, where either one or two $(OH)^-$ were lost at a time [8, 9, 26]. However, no structural reasons have been shown to cause this stepwise decomposition [10]. All OH sites in the jarosite structure are crystallographically

equivalent, and there exists no structural reason or relation between the jarosite parent structure and the structure of the decomposition products hematite and yavapaiite that would cause some $(OH)^-$ groups to leave the structure preferentially. The stepwise decomposition was also not observed in the current work; the $(OH)^-$ loss step showed very little internal structure. The behavior repeatedly observed by Frost and co-workers may be an issue associated with the physical form of the material, e.g., particle size. Large quantities of material may provide variable diffusional resistance to the loss of $(OH)^-$, and using very small amounts in the present study minimized this effect. The single particular feature observed here is a characteristic change in the $d\alpha/dt$ (or dm/dt) peak shape as the heating rate increases. To illustrate this, Figure 2.9 shows the derivative of the mass loss curves associated with the $(OH)^-$ decomposition. At low heating rates there is one symmetric peak with a shoulder on the high-temperature side. With increasing heating rate, this shoulder becomes stronger until it constitutes the majority of the peak.

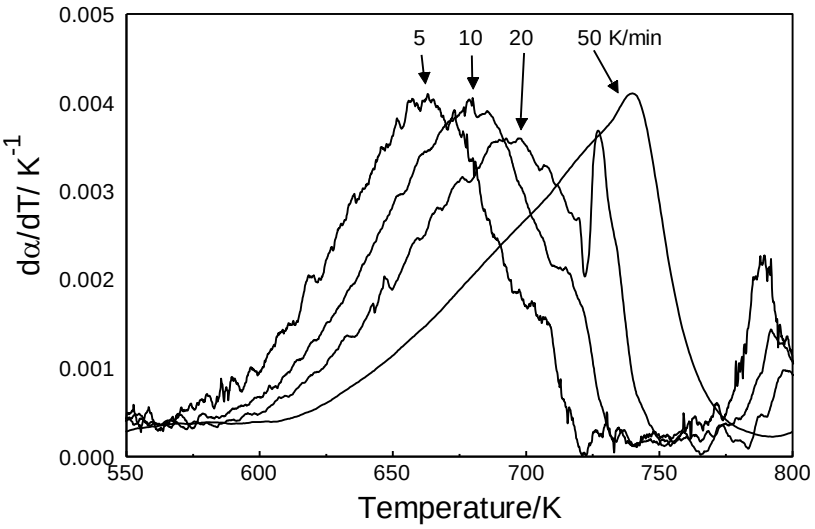

Figure 2.9 Mass-loss derivative curves at varying heating rates associated with the loss of $(OH)^-$.

This suggests the contribution of two reactions to the $(OH)^-$ loss step, although the proportions between the two are not constant, and can therefore not be ascribed to set amounts of $(OH)^-$. The apparent activation energy in Figure 2.8 for the global α range 0.05-0.35 shows a slight decrease, suggesting higher activation energy for the first, and a lower activation energy for the later reaction.

To understand the mechanism that describes the $(OH)^-$ loss, $y(\alpha)$ and $z(\alpha)$ were calculated [24], the local α value at the maxima for these two curves were at 0 and ~0.86 for different heating rates. As per the suggestion in reference [24], a two dimensional diffusion model was initially used to describe the decomposition, this model had difficulty in describing the observed curve and also the model failed to describe the change in the nature of the decomposition seen at higher heating rates (see Figure 2.9). Hence an alternative approach was explored to describe the observed curves.

The behavior in Figure 2.9 can be replicated if a change in reaction mechanism is assumed. Such a change could, for example, occur if at higher reaction rates, diffusion

becomes rate limiting. To formulate this behavior, the $(OH)^-$ loss was modeled as a sequence of two reactions, where only the second reaction carries the mass loss associated with all $(OH)^-$ present in the jarosite. In this scenario both reactions always occur, but the first reaction is rate limiting at low heating rates while the second reaction is rate limiting at higher heating rates. The overall mass difference between before and after the steps is independent of which reaction is rate limiting. Therefore the mass loss observable in the TG experiment can only be assigned to the total of both reactions. This was achieved by setting the molar mass of the product of the first reaction to zero for the purpose of computing the global α according to Equation 2.3. At the same time, the molar mass was not changed for the purpose of computing the amount of material available for the follow-on reaction (Equation. 2.4).

2.3.3.3 $(SO_4)^{2-}$ Groups. The $(SO_4)^{2-}$ is lost from the products of the $(OH)^-$ loss, β-Fe_2O_3 , $Fe(SO_4)(OH)$, and $KFe(SO_4)_2$. Only the latter two contribute to the mass loss. The final decomposition products are Fe_2O_3 and K_2SO_4.

The loss of the $(SO_4)^{2-}$ groups shows considerably more features than the $(OH)^-$ loss. It starts with a small mass loss step near 750 K (at 5 K/min), which appears to have a high activation energy, and becomes less pronounced at higher heating rates. Figure 2.10 shows the derivative of the mass loss curves associated with this step. The activation energy of this step is not easily distinguished in Figure 2.8, but it can be approximated using Kissinger processing for the peaks shown in Figure 2.9 [27]. Plotting $\ln(\beta/T_{max}^2)$ vs. $1/T_{max}$ where β is the heating rate and T_{max} is the peak maximum

in Figure 2.10 (the plot is omitted for brevity), one obtains a rather high apparent activation energy of 522 ± 0.56 kJ/mol.

From previous investigations it is known that the $(OH)^-$ decomposition step results in the formation of amorphous Fe_2O_3, which then proceeds to crystallize in this temperature range [15]. While this crystallization is neutral with respect to thermogravimetry, it may indirectly affect the loss of SO_3 from the remaining of material. The following scenario described by Equation 2.6, while speculative, is consistent with the observations: The behavior shown in Figure 2.10 can be replicated by taking the pre-exponential factor of the SO_3 loss step as a function of the degree of crystallization of the amorphous Fe_2O_3. This idea can be rationalized by assuming that the change in Fe_2O_3 crystallinity causes the permeability of the partially decomposed material to change, so that the gaseous decomposition product SO_3 is removed more easily.

$$\log(A_{SO_3}) = a + b \cdot \left(1 - \alpha_{Fe_2O_3}\right) \tag{2.6}$$

The parameters *a* and *b* are treated as adjustable parameters, and chosen to best match the observed mass loss curves. Note that the high-activation energy process reflects the crystallization of Fe_2O_3, which affects the decomposition of SO_3 only indirectly.

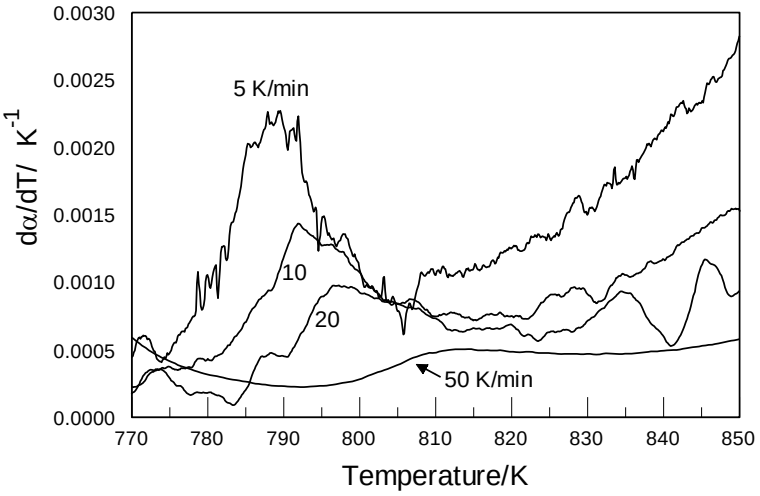

Figure 2.10 Mass-loss derivative curves at varying heating rates at the onset of the SO_4^{2-} loss.

At higher temperatures, there is a slope change in the SO_3 loss step, which is more distinct in the constant-reaction rate measurements (see Figure 2.4). This is an indication that the SO_3 loss reaction can not be treated as a single-stage reaction, but consists itself of subreactions. XRD analysis showed the material at the slope change to consist of Fe_2O_3 and $K_3Fe(SO_4)_3$. Assuming that all K that was present in the $KFe(SO_4)_2$ of the products of OH decomposition is present in the intermediate $K_3Fe(SO_4)_3$, and that it will occur in the final decomposition product as K_2SO_4, one can postulate the following sequence:

$$KFe(SO_4)_2 \rightarrow 1/3\ K_3Fe(SO_4)_3 + 1/3\ Fe_2O_3 + SO_3 \rightarrow ½\ K_2SO_4 + ½\ Fe_2O_3 + 1.5\ SO_3$$

Where one mole of SO_3 is lost in the first step, and one-half mole is lost in the final step, resulting in the total loss of 1.5 moles. This suggests that the size of the first step should be twice the size of the final step. This is confirmed by the well-resolved constant-reaction rate measurement (Figure 2.4). Therefore, the SO_3 loss step was modeled as two sequential reactions with the mass losses corresponding to SO_3 and ½

SO_3, respectively. The onset of the first reaction is further influenced by the crystallization of Fe_2O_3, which itself carries no mass loss.

As mentioned, the activation energy for the first part of the SO_3 loss step was taken from the isoconversion analysis (see Figure 2.8), and the activation energy of the second step was adjusted so that the calculated mass loss matches the observed curves.

2.3.3.4 Hydronium Component. The hydronium component carries $(OH)^-$, $(SO_4)^{2-}$, and $(H_3O)^+$ as volatile constituents. The loss of $(OH)^-$ cannot usefully be distinguished from that of the potassium component, and so its treatment is subsumed into the overall $(OH)^-$ loss step described above.

Unlike for K-jarosite, a hydronium analog of the product of the $(OH)^-$ loss, $KFe(SO_4)_2$ yavapaiite, does not exist, and so the SO_3 loss can not similarly be accounted for together with the SO_3 loss of the K component. However, the amount of H_3O and associated SO_3 is so small that it also can not be usefully resolved as an individual decomposition step from the thermogravimetric curves. Therefore, it is being treated as one step, where SO_3 and H_2O are lost simultaneously, in parallel to the SO_3 loss of the K component. In essence, it is carried here only to account for the mass balance. It is never explicitly distinguished.

2.3.3.5 "Vacancy Component". As pointed out in section 2.3.3, the virtual "vacancy component" was assumed to completely decompose together with the other $(OH)^-$ loss reactions. Hence, the associated mass loss was subsumed with the mass loss due to OH^-

removal from all components. Like the hydronium component, it is only carried to account for the mass balance, and it is also not explicitly distinguished.

The relations described above are summarized in the reaction scheme illustrated in Figure 2.11. Kinetic parameters are shown in Table 2.1. Uncertainties are generally close to 0.001 for the α-ranges, and the activation energies were taken with a resolution of 5 kJ/mol. With the model described above, and the kinetic parameters shown in Table 2.1, decomposition curves were calculated. The result is shown in Figure 2.12. Experimental and calculated curves are very close to each other over the entire temperature range; the effect of heating rate is also well accounted for in the model.

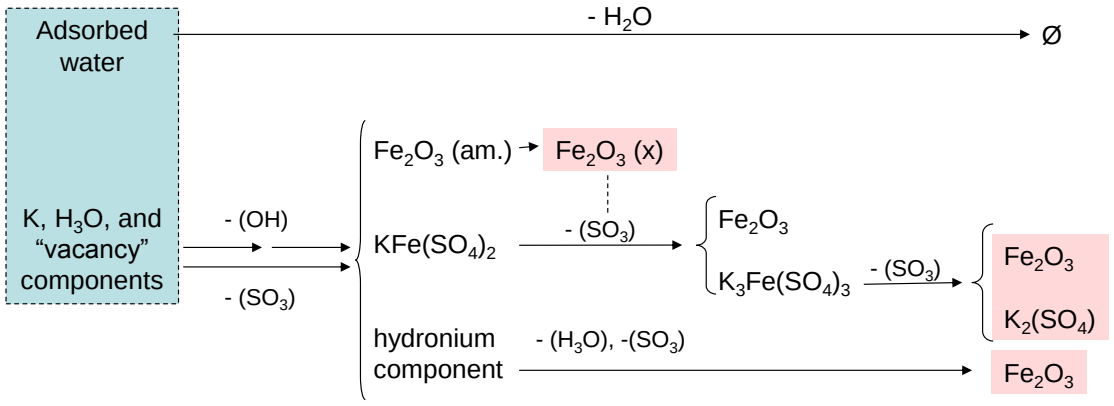

Figure 2.11 Reaction scheme of jarosite thermal decomposition.

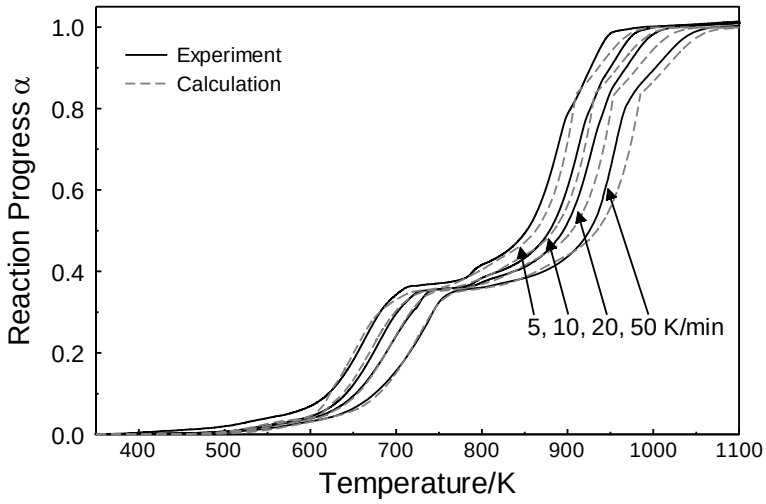

Figure 2.12 Comparison between observed and calculated decomposition of K-jarosite.

Table 2.1 Kinetic Parameters used in the Reaction Scheme Shown in Figure 2.11

	Associated mass loss in units of global α	Activation energy / kJ/mol	Pre-exponential factor / log(A)	Reaction model
Loss of adsorbed water	0.034	150	11	$4.431 \cdot (1-\alpha)^{0.951} \cdot \alpha^{-1.004}$ [c]
Loss of $(OH)^-$, first step carrying no mass loss	–	250 [a]	18.2	$(1-\alpha)$
Loss of $(OH)^-$, second step	0.287	125 [b]	7.5	$(1-\alpha)$
SO_3 loss from the "vacancy component"	0.019	–		
Crystallization of Fe_2O_3 carrying no mass loss	–	525 [b]	33	$(1-\alpha)$
Loss of SO_3 from $KFe(SO_4)_2$	0.400	215 [a]	$a = 9.5$ [d] $b = 0.85$ [d]	$(1-\alpha)^0 = 1$
SO_3 loss from the hydronium component	0.059	–		
Loss of SO_3 from $K_3Fe(SO_4)_3$	0.200	220 (fitting)	9.5	$(1-\alpha)$

a) determined from isoconversion analysis
b) determined from Kissinger-analysis of peaks in dm/dt
c) approximation of a three-dimensional diffusion model [28]
d) coefficients for Equation 2.6

2.4 Discussion

The model in this study was developed to provide a practical tool for the use of jarosites as thermal witness materials. Ultimately, it is hoped that thermal histories, described by a small number of parameters, can be reconstructed by quantifying the partial progress of individual subreactions of the jarosite decomposition. A thermal history could, for example, be described by two parameters: a constant temperature and a holding time. Reconstruction of this thermal history would require tracking at least two independent subreactions. The more subreactions are available for observation, the more complex thermal histories can be reconstructed, at least in principle. With this background, the present model has a number of advantages as well as shortcomings. The model uses the traditional concept of the kinetic triplet (pre-exponential factor, constant activation energy, conversion-based reaction model) in favor of more mechanistic models considering particle radii, and the diffusion of volatile decomposition products through growing layers of solid decomposition products.

The description used in the model also implicitly assumes that the driving force for each subreaction is invariant. This implies that according to the present model, intermediate decomposition products (e.g., the yavapaiite phase) are only *kinetically* prevented from further decomposing even under conditions where the phase would be *thermodynamically* stable. The reaction model chosen for most of the subreactions is the first order reaction, a linear dependence of the reaction rate on the degree of conversion.

The decision to base the model on constant kinetic triplets for the subreactions was made in light of the available observables *vs*. the required parameters to describe the model. As it is, one can argue that the decomposition curves shown in Figure 2.4 show

about six distinguishable features, that is, six mass loss steps that under ideal conditions can each be assigned a mass change, a reference temperature, and through analysis of the effect of heating rates, an activation energy. This provides at best 6×3=18 observables.

At the same time, the decomposition model as outlined in Figure 2.10 consists of nine subreactions, necessitated in part by the particular composition of the material used: (loss of) adsorbed water (1 subreaction), $(OH)^-$ groups in two distinguishable steps (2), SO_3 in two distinguishable steps (2), $(H_3O)^+$ from the hydronium component (1), SO_3 from the hydronium component (1), SO_3 from the vacancy component (1), and the crystallization of amorphous Fe_2O_3 (1). Using the paradigm of the constant kinetic triplet, each of the subreactions requires three numerical parameters to describe it quantitatively: an associated mass change, a pre-exponential factor, and activation energy. In addition, there are choices for the decomposition model and it can be considered an additional parameter. This means that the model in its current form requires 9×4=36 parameters. Clearly, and regardless of the details, the model is severely underconstrained even disregarding measurement noise and experimental uncertainty. A number of simplifying assumptions are necessary. The simplest assumption was to use first order reactions as the default reaction model. While not providing much mechanistic insight in the particle decomposition, this provides for generally valid behavior of declining reaction rates as the reactant is being depleted. Further assumptions such as lumping the SO_3 and $(H_3O)^+$ losses of the hydronium component with the K component are justified by realizing their minor although not completely negligible contribution to the overall mass change.

Finally, as stated in the introduction, the work was motivated by the need for particulate thermal witness materials in the context of biological agent defeat applications. It aimed for a practical model that could be used to evaluate transient high-temperature environments. The time scales involved are on the order of a second or less, and if a given decomposition subreaction occurs on this time scale, it will be at a higher temperature than what was observed in the present study. As a result, the decomposition will occur further from any thermodynamic equilibrium than in a thermoanalysis experiment. The issue of kinetic vs. thermodynamic stability is therefore unlikely to be relevant in the targeted application.

The decomposition model developed here can now be applied to jarosite for use as thermal witness material. The main benefit is the fact that jarosite is ubiquitous and relatively cheap. However, in the strictest sense, the kinetic parameters shown in

Table 2.1 are only valid for the specific material synthesized here. Natural material, or synthetic material with different composition (e.g., amount of $(H_3O)^+$), or material with substantially different particle sizes will require updated kinetic parameters. Jarosites with identical composition but different vacancy ordering states would likely affect the model only as far as minor changes in the activation energies. Nevertheless, the general decomposition scheme shown in Figure 2.11 is expected to remain valid, and the methodology outlined in the present work should make the derivation of updated kinetic parameters a straightforward task.

Using the decomposition scheme developed here, it should be possible to apply the observed decomposition steps to other jarosite group minerals. Since the K site can accommodate a wide variety of cations – e.g., Na, NH_4, Ag, Pb, and the Fe site can substitute Al, a variety of decomposition reactions should be expected. Current results, in agreement with previous work (e.g., [8, 9, 26]) suggest that the overall sequence of adsorbed water – $(OH)^-$ groups – $(SO_4)^{2-}$ groups will be preserved. Also, the initial loss of adsorbed water will probably vary little with composition. The following loss of the $(OH)^-$ and the $(SO_4)^{2-}$ groups likely depends on the existence and stability of the respective intermediate decomposition products, Fe_2O_3 and yavapaiite in the present study. If analogous phases don't exist, such as the case with pure $(H_3O)^+$ jarosite, then the $(OH)^-$ loss step may induce further collapse of intermediate structures, and the main steps of $(OH)^-$ and $(SO_4)^{2-}$ loss may be less clearly separated, although earlier work on H_3O and NH_4 jarosite ([8, 26]) suggest that the general sequence remains preserved.

2.5 Conclusion

A complex model for the decomposition of K-H_3O jarosite was established based on thermoanalysis data up to temperatures of 1100 K. Individual decomposition steps describe the loss of $(OH)^-$ groups, SO_3, adsorbed water, and the crystallization of amorphous Fe_2O_3. Major solid intermediate products are $KFe(SO_4)_2$, yavapaiite, amorphous, β- and α-Fe_2O_3, and $K_3Fe(SO_4)_3$. Final products are α-Fe_2O_3 and K_2SO_4. The model combines sequential and parallel individual reactions and the reactions are described using constant kinetic triplets. Activation energies were estimated from isoconversion analysis and pre-exponential factors were adjusted to match the observed decomposition curves. Individual reaction models, based on the degree of conversion of the individual reactions, were left at first-order where possible. Despite these simplifications, the model well describes the present experiments and is broadly consistent with previously reported decomposition behavior of K-jarosite and H_3O-jarosite.

CHAPTER 3

EVALUATION OF K-JAROSITE AS THERMAL WITNESS MATERIAL

3.1 Introduction

Explosions generate short-lived, high-temperature dynamic environments encountered in various practical applications. Advanced energetic formulations and designs of explosive charges enable one to vary spatial and temporal temperature distributions inside the generated fire balls[29-31] Quantitative measurements of such temperature distributions are necessary to validate, optimize, and improve the state of the art energetic systems and components. However, the interiors of combustion clouds are not easily accessible for temperature measurements. Conventional temperature sensors such as thermocouples are either too large, and therefore, sluggish to faithfully record the true temperature-time histories, or they are too fragile and become damaged due to the strong pressure effects associated with explosions. Similarly, since explosive-generated combustion clouds generally consist of incandescent aerosols and are therefore optically thick [32], spectroscopic methods for temperature measurements can only sense the exterior surface of the combustion cloud. The unique challenge to accurately record temperature-time histories where times are on the scale of seconds or less, and temperatures can be as high as 1500-2000 K, motivated the development of a variety of particulate temperature sensors that are injected in the combustion cloud, and function as witness materials (e.g., ref. [33]). It is desired that the particles are small enough to be readily dispersed. The general concept requires recovery of the sensor particles after the combustion event, and their interrogation. The extent of the change undergone during the combustion event is then correlated with the temperature-time history experienced by the particles.

While some effort has been directed at the development of engineered particles [33-35], the current manuscript examines a natural material for the potential use as a particulate thermal witness material. Minerals of the jarosite group are complex sulfate-hydrates that undergo a set of distinct decomposition steps when heated [8, 9, 36]. Jarosite particles that are exposed to high temperatures in a combustion event may partially decompose. If this partially decomposed material is recovered, it can be studied by thermal analysis to determine its residual decomposition. In a previous investigation, a quantitative decomposition model has been developed for K-H_3O jarosite, (K, H_3O)$Fe_3(SO_4)_2(OH)_6 \cdot xH_2O$, that allows to compute its partial decomposition under arbitrary time-temperature conditions as well as the residual decomposition of partially decomposed material [37]. It becomes possible to infer the temperature history experienced by the witness material correlating its experimentally observed residual decomposition with one calculated for an assumed time-temperature profile.

At a minimum, two parameters are required to describe a temperature history, e.g., a constant temperature and time duration. More detailed time-temperature profiles, including for example, an initial heating ramp, or a cooling rate, require more parameters. Several processes occur during thermal decomposition of K-H_3O jarosite. Adsorbed water, $(OH)^-$ groups, and SO_3 are lost in sequence. For the loss of $(OH)^-$ and SO_3, further sub-reactions can be identified [37]. It is expected that quantifying more of such sub-reactions of the overall jarosite decomposition helps one to characterize the respective time-temperature profile in more detail. In reality, one is likely limited by how accurately individual sub-reactions can be quantified. The current manuscript aims to examine experimentally how well details of the jarosite thermal decomposition can be

correlated with a recovered time-temperature profile. Aerosolized jarosite particles are partially decomposed in air under well-characterized time-temperature profiles, and subsequently examined while being fully decomposed using thermogravimetry. In particular, this study will show whether the recently developed kinetic model applies to high-heating rate situations, and what time and temperature resolution can be expected.

3.2 Experimental Setup

Details of the synthesis and characterization of K-H_3O jarosite have been reported previously [37]. To summarize, the material was synthesized by a wet chemical method, its composition was determined by a combination of x-ray diffraction measurements and mass balance considerations, and the particle size was reduced by treating it as an aqueous slurry in a roller mill. Finally, the material was dried at 100 °C under mild vacuum for 18 hours. The actual composition of the as-synthesized material was determined as $(H_3O)_{0.058}K_{0.92}Fe_{2.96}(SO_4)_2(OH)_{5.858}\cdot 0.35\ H_2O$. The particle size distribution, as determined by laser light scattering, ranges between 1 and 20 μm, with a volumetric mean at 5.32 μm [37].

Rapid heating experiments were performed in a vertically mounted 1350-W Bransted/Thermolyne tube furnace, Type 21100 Thermo Scientific. A 1 inch ID sintered alumina tube was inserted in the furnace. The heated section was 300 mm long. The top of the alumina tube was capped with a block of aluminum to which a gas feed line was connected. Aerosolized particles were fed from the top, and collected at the bottom of the flow furnace. Figure 3.1 shows a schematic illustration of the experimental setup.

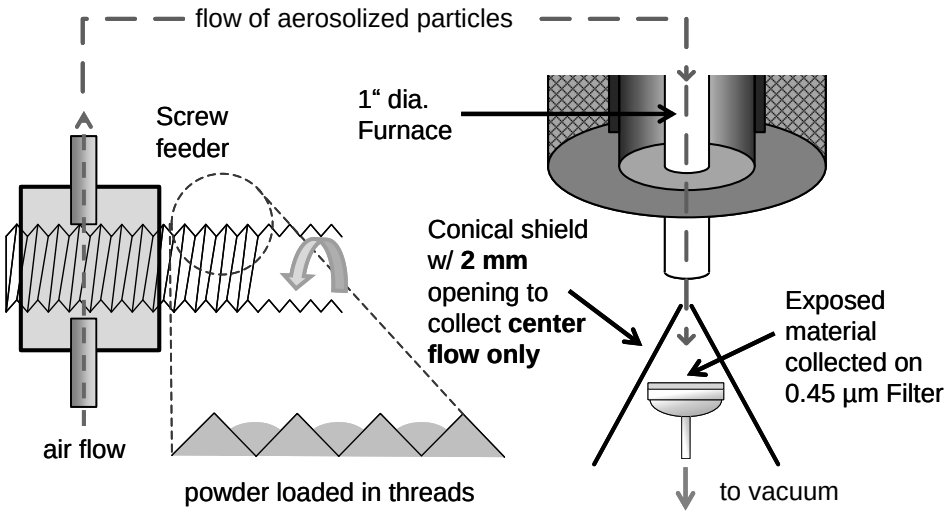

Figure 3.1 Schematic illustration of the rapid heating experiment.

Particles were aerosolized using a custom-built screw particle feeder. Jarosite powder was coated as an aqueous slurry onto the threads of a ¾ in. diameter screw with 16 threads per inch. The coated screw was dried at 60 °C for three hours in a mild vacuum, and then fit snugly into a brass tube with connections that allows for an air stream directed tangentially at the powder. A motor rotates the screw slowly to continually expose fresh powder to the air stream, and the air entrains the powder, carrying it to the flow furnace. This design allows control of the aerosol density by control of the screw rotation rate independent of the flow rate of the carrier air.

Since there is some air leaking in the axial direction of the screw, some pressure loss occurs, and it was necessary to determine the actual gas flow rate delivered to the flow furnace. This was measured using a Singer DTM-115 Diaphragm Gas Meter. These measurements were performed with the screw feeder assembled, but without powder loaded. Volumetric flow rates varied from 650 – 830 mL/min.

To achieve a laminar flow of aerosol in the furnace, the aerosol from the feeder was injected into the furnace approximately three furnace diameters upstream from the

actual heated section. An established laminar flow in the furnace implies radial variations of temperature as well as velocity. Temperatures in the center of the tube are lower and velocities are higher than their respective values close to the wall. Particles traveling along the axis therefore experience a shorter exposure at lower temperatures compared to particles traveling close to the wall. Preliminary computations using Fluent [ANSYS® Academic Research] were carried out to gauge this effect; results are shown in Figure 3.2.

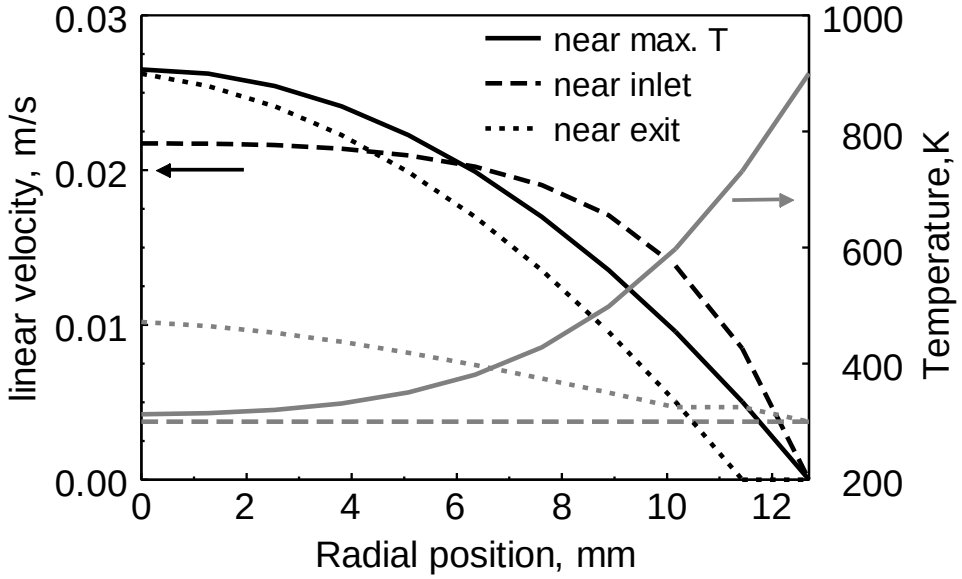

Figure 3.2 Radial profiles of flow velocity and temperature at the entrance and exit of the flow furnace, and close to the peak temperature.

This preliminary assessment shows that velocity and temperature vary least closest to the axis of the flow furnace. Therefore, a conical metal shield was installed at the exit (see Figure 3.1) to screen out everything but an area with 2 mm diameter in the center of the flow. In this region, temperature variations were less than 2 %, and velocity

variations less than 5 %. The aerosol passing through this shield was pulled through a 0.45 μm filter by vacuum.

The temperature along the furnace axis was determined for several settings using a K-type thermocouple by Omega Engineering. The temperature measurements were done with gas flow, but without aerosolized jarosite particles. The thermocouple was calibrated by an infrared high temperature black body source by Omega (BB-4A – 100 °C – 982 °C). Additional corrections were done by accounting for the temperature at the thermocouple reference junction during measurements.

The temperature and velocity measurements are transposed into a time-temperature profile experienced by the particle along the length of the flow furnace. The linear air flow is corrected by the volumetric expansion at the respective temperature of the flow furnace assuming behavior as ideal gas. Additionally, particle velocity is corrected by accounting for settling velocity. Figure 3.3 illustrates the temperature-time profiles for three different operating conditions. At time zero, the particles enter the tube furnace. The total time spent by the particles in the tube furnace is referred to as the residence time. The operating conditions of all five experiments performed with the jarosite aerosol fed through the furnace are shown in Table 3.1.

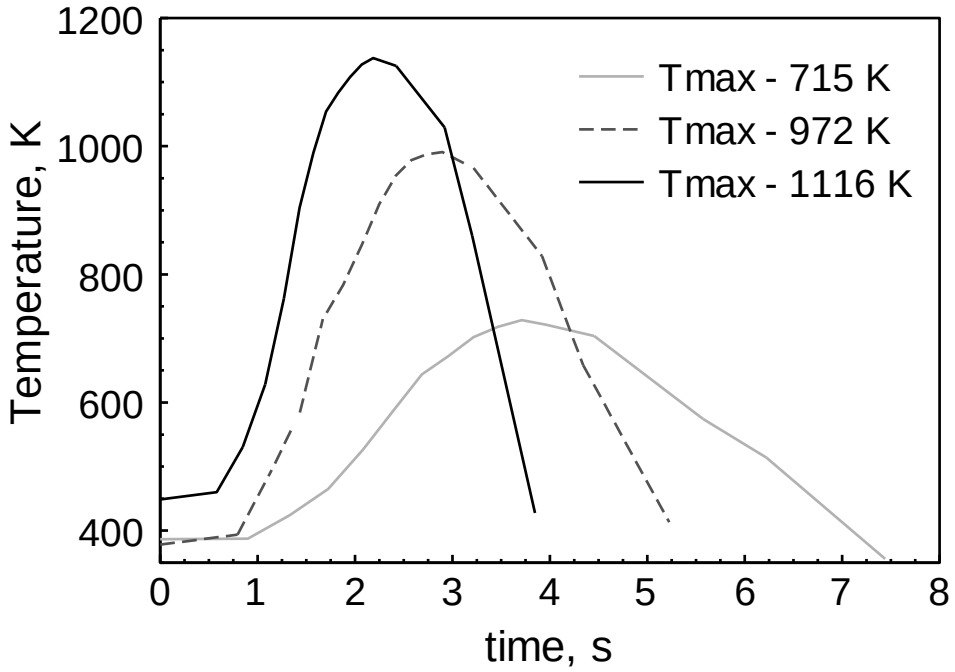

Figure 3.3 Time-temperature profiles along the axis of the flow furnace.

Table 3.1 Operating Conditions of the Tube Furnace

Measured maximum Temperature, K	**Volumetric flow rate, mL/min**	**Residence time, s**
715	637	7.442
756	799	5.627
854	692	6.181
972	726	5.225
1116	854	3.847

After collection, the partially decomposed jarosite particles were recovered from the filter and residual decomposition was recorded by thermogravimetric analysis (TG) using a TA Instruments model Q5000IR thermo-gravimetric analyzer. The balance was purged with argon (Matheson Tri-Gas, 99.999%) at 10 ml/min and the furnace was purged with air (Airgas, zero grade) at 25 ml/min. Alumina pans were used. The instrument was calibrated using the Curie points of alumel, nickel, and cobalt and the

melting points of indium, tin, bismuth, zinc, and aluminum. The calibration was performed at heating rates ranging from 5 to 200 K/min.

The amount of material collected from the flow furnace experiments is very small. Typical mass of material used to determine residual decomposition varied from 0.5-0.8 mg. Since at these low masses signal drift becomes significant, a baseline was recorded immediately after each experiment without opening the TG or disturbing the now completely decomposed sample in any way. This baseline measurement was then subtracted from the actual measurement.

3.3 Model Computation

Parallel to the experimental partial decomposition in the flow furnace, the previously determined decomposition model [37] was used to calculate the expected partial decomposition under the time-temperature profiles illustrated in Figure 3.4, as well as the residual decomposition of the recovered material by TG.

The decomposition model considers the K-H_3O jarosite a composite of three components which decompose in parallel and independent of each other: ideal K-jarosite, ideal H_3O-jarosite, and a hypothetical vacancy component. Of these three, the K component contributes most significantly to the overall weight loss during decomposition. From this component, $(OH)^-$ and SO_3 groups are lost in sequence. The loss of $(OH)^-$ was described by two interdependent parallel reactions to account for a possible shift in reaction mechanism as the heating rate increases. The SO_3 loss was divided in two sequential steps to account for an additional stoichiometric phase observed during decomposition. For further details, see ref. [37].

The result of these calculations is illustrated in Figure 3.4. The figure shows the reaction progress α (α=1 corresponds to fully decomposed jarosite) vs. temperature. The solid curve shows the decomposition predicted to occur as the particles pass through the furnace. The dashed curve shows the residual decomposition as expected to occur in a TG experiment under linear heating conditions with a heating rate of 5 K/min. The shape of the dashed curve is not only affected by the final value of α achieved as a result of decomposition in the flow furnace, but also by the specific decomposition scenario (determined by the *T(t)* profile of the flow furnace.) Thus, inspecting such residual decomposition curves can be used to recover *T(t)* profiles.

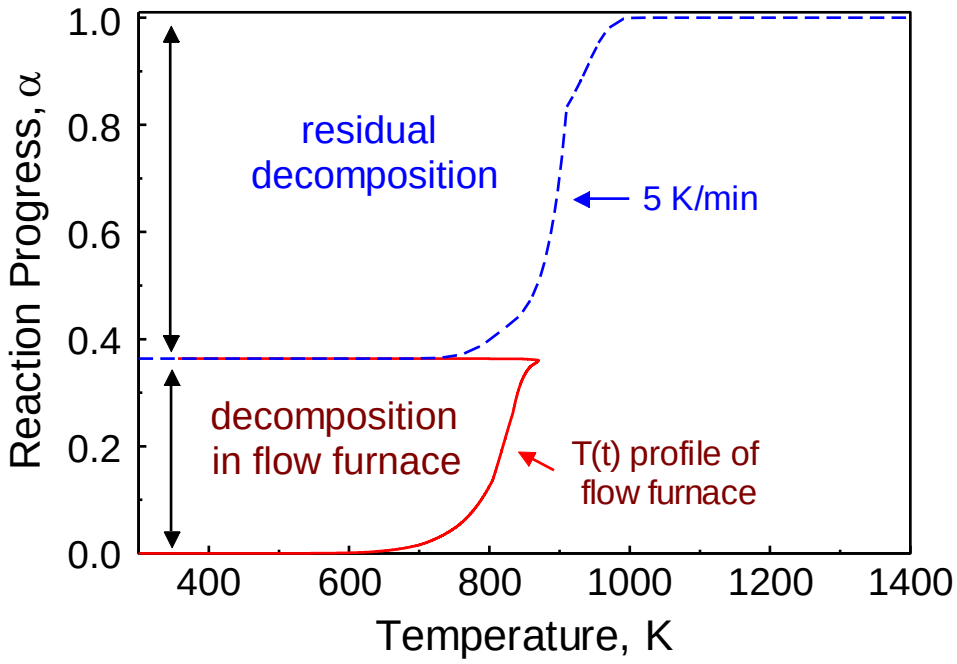

Figure 3.4 Calculated decomposition of jarosite during exposure in the flow furnace (solid), and residual decomposition recorded by TG (dashed).

3.3.1 Thermal Lag

Prior to examining the theoretically possible resolution achievable with a material like this, one should justify that there is no significant temperature distribution within a single particle at the heating rates encountered in the experiment. Equation (3.1) describes the characteristic equilibration time, *t*, for a cold particle inserted into a hot gas based on a lumped capacitance model.

$$t = \frac{\rho V c}{h A_s} \ln\left(\frac{T_i - T_\infty}{T - T_\infty}\right) \tag{3.1}$$

Here, ρ is the density, V is the volume, c is the heat capacity, and A_s is the surface area of the particle, and h is the temperature-dependent heat transfer coefficient of air. The coefficient of heat transfer can be estimated from the Nusselt number:

$$Nu = \frac{hL}{k_{Air}} \tag{3.2}$$

Where L is a characteristic length and k_{Air} is the temperature-dependent thermal conductivity of air. The Nusselt number of a 10-µm particle in air is reasonably close to two [38]. With a thermal conductivity of air at 900 K of 62 mW/(m·K) [39], and using the ratio of volume over surface area of a sphere, this yields approximately $7.4 \cdot 10^4$ W/(m^{2}K) for h. Since in the lumped capacitance model the particle temperature, T, approaches the environment temperature, T_∞, exponentially, one has to choose an arbitrary target temperature, T_i, that will be reached in time t. Setting the environment temperature to 900 K, and the target temperature to 899 K leaves an acceptable temperature error of 1 K. With these parameters, a 10 µm particle takes about 0.3 ms,

and a 100 µm particle takes about 30 ms to heat to within 1 K of the environment. These time scales are of the order of a percent or less of the experimental time scales involved (see Figure 3.3), and the assumption that the particle temperature does not lag significantly behind the environment temperature is valid for the present experiment. These time scales are shorter than the time scale of the current experiments, but not by orders of magnitude.

Further, temperature gradients are possible between the surface and the core of the particle. This phenomenon can be quantified by the Biot number (Bi) Equation (3.3).

$$Bi = \frac{hL_c}{k_B} \tag{3.3}$$

Where h is the heat transfer coefficient of air at 300 K (h increases with temperature, and to estimate the worst case scenario we assume the value at 300K rather than 900K), L_c is the characteristic length of the particle (ratio of volume to surface area of the particle) and k_B is the thermal conductivity of the material. The thermal conductivity of jarosite and its decomposition products was conservatively estimated to k_B =1 W/m/K. Literature data is scarce, this value is typical for non-metallic materials [40]. Fe_2O_3 as one of the decomposition products is reported to have a thermal conductivity above 5 W/(mK) in the relevant temperature range [41], and a related sulfate – Li_2SO_4 – [42] exceeds 1 W/(mK) at all temperatures.

The Biot number was calculated as a function of temperature by inserting a room-temperature particle into an environment of 1000 K, accounting for temperature-dependent particle heat capacity and thermal conductivity of air. Both, this scenario and the assumed thermal conductivity, represent therefore a worst-case estimate for the Biot

number. The resulting Biot number is 0.03 at its highest. With a Biot number of less than 0.1 it can be assumed that internal thermal variations are less than 5 % [39]. The value estimated here is well within this margin, and therefore internal thermal gradients can be neglected. The experiments therefore reasonably approach realistic heating conditions in a combustion environment.

3.3.2 Sensitivity Analysis

From a set of basic calculations, it is now possible to estimate the time-temperature resolution that can be expected from inspecting the residual decomposition curves.

The axial temperature profiles of the flow furnace, *T(x)*, with *x* as the distance from the inlet, was approximated by a polynomial fit so that

$$T(x) = T_{\max} \cdot f(x) \tag{3.4}$$

where T_{max} is the maximum temperature and $f(x)$ is a polynomial that depends only on the distance *x*. The parameters for $f(x)$ were obtained by curve fitting. Further, the temperature-dependent relation between distance *x* and time *t* was determined by considering that

$$\frac{dx}{dt} = \frac{v_0}{A} \cdot \frac{T(x)}{T_0} + \frac{g \cdot d_p^2}{18\mu_{\text{Air}}}\left(\rho_p - \rho_{\text{Air}}\right) \tag{3.5}$$

where v_0 is the flow rate of the room temperature air flow from the particle feeder, *A* is the cross-sectional area of the furnace tube, and T_0 is the room temperature.

The first term on the right hand side is therefore the linear flow velocity in the furnace, corrected for the thermal expansion of the air. The second term on the RHS of Equation 3.4 is the terminal settling velocity of the particles with g as the gravitational constant, d_p the particle diameter taken as the average diameter of 5 μm [37], ρ_p the density of jarosite (3 g/cm^3), and μ_{Air} and ρ_{Air} are the temperature-dependent values of the viscosity and density of air, respectively. As noted above, particles and air were taken as being at the same temperature. Equation (3.3) was then numerically integrated to obtain the particle temperature as a function of time.

Equations (3.4) and (3.5) contain only two parameters that are readily varied in the experiment: the base flow rate v_0 and the maximum temperature T_{max}. Both of those parameters affect the total weight loss. The effects of v_0 and T_{max} are correlated; higher values of v_0 require higher T_{max} to achieve a given decomposition of the exposed particle. In other words, in the space defined by v_0 and T_{max}, there exist curves of constant total weight loss during partial decomposition. These curves were calculated based on the current decomposition model, and are illustrated in Figure 3.5. The curves show that any given overall decomposition can be achieved by a combination of base flow rate and maximum temperature that fall on the respective curve.

As a way to assess the resolution of the kinetic decomposition model for time-temperature forensics, it is now reasonable to ask what kind of resolution in the TG-residual decomposition measurements is needed in order to discriminate different conditions that result in the same overall degree of decomposition. Taking two different points on one curve in Figure 3.5, for example, how different are the TG residual decomposition traces expected to be? Conversely, how different should v_0 and T_{max} for

those two points be so that their respective residual decomposition traces can be readily distinguished in a typical TG experiment?

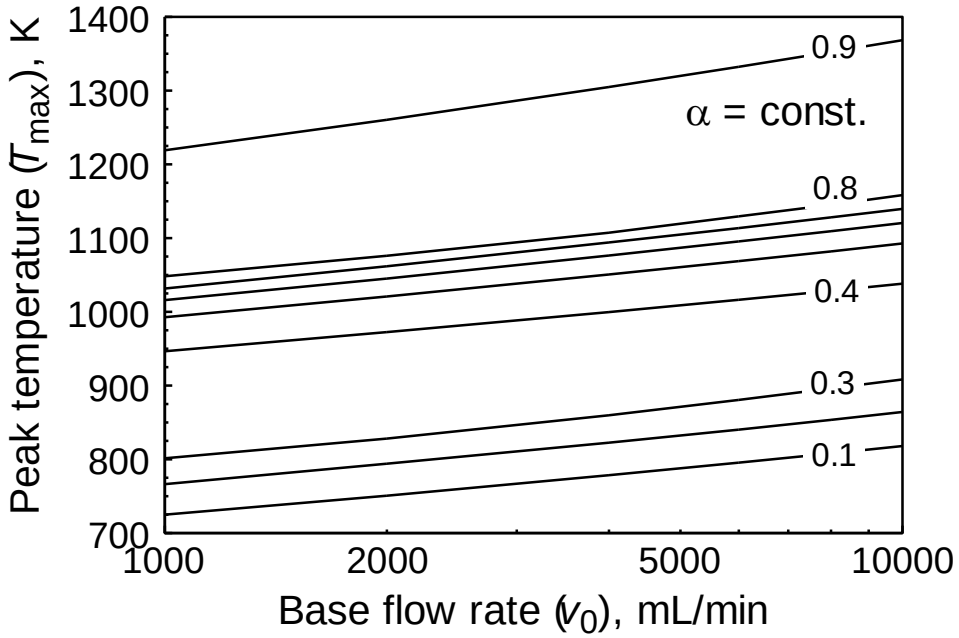

Figure 3.5 Parameter space of peak temperature and base flow rate with curves of constant overall decomposition.

The analysis is illustrated in Figure 3.6 where exposure conditions were selected based on the experimental configuration used in the present project. The top portion shows two residual decomposition curves computed for two flow furnace conditions that differ by a temperature difference of $\Delta T = 100$ K. The base flow rate v_0 is chosen for each temperature so that the overall degree of decomposition in the flow furnace is the same for both experiments. The bottom part of Figure 3.6 shows the difference between those two curves. To compare multiple exposure conditions, this difference curve can further be reduced to one scalar value, its maximum amplitude or maximum mass ratio difference, Δm. The sensitivity of the TG interrogation of the exposed samples can now

be assessed considering how Δm (for a constant α) is affected by changes in either T_{max} or v_0.

First, a set of benchmark conditions are selected with a fixed v_0 of 800 mL/min and with T_{max} ranging from 700 K to 1200 K. For each condition in this set, two calculations for Δm are performed. In one case, T_{max} is increased by 100 K and v_0 is adjusted to maintain the value of α of the respective benchmark condition. The resulting Δm is calculated. Second, starting from the same benchmark condition, v_0 is increased by a factor of 10 and T_{max} is adjusted to maintain constant α. The results of both sets of calculations are shown in Figure 3.7, illustrating the resolution required in residual decomposition measurements in order to discriminate conditions in the flow furnace where peak temperatures are different by ΔT_{max} = 100 K (filled bullets), or where base flow rates v_0 are different by a factor of 10 (open squares).

The effects of both changes: T_{max} + 100 K and $v_0 \cdot 10$, are nearly identical. At best, TGA measurements of residual decomposition with accuracy better than about 1 wt-% need to be performed to resolve either change. Further, this resolution requirement applies only to a temperature range between about 750 and 830 K. Outside this range, the resolution requirement quickly drops to below 0.1 wt-%.

To illustrate how this sensitivity relates to the details of the decomposition model, the dashed line in Figure 3.7 shows the values of α corresponding to the benchmark conditions T_{max} and v_0 = 800 mL/min. This curve is schematically very similar to the TG measurements used to derive the kinetic model, and published previously [37], in that it shows defined stages that can be attributed to individual reactions. The decomposition step seen below about 850 K corresponds to the loss of $(OH)^-$ groups from the jarosite

structure. The step near 1000 K corresponds to the first stage of the SO_3 loss, followed by the second stage of SO_3 loss above about 1030 K. The highest sensitivity in the temperature range 750 – 830 K therefore, coincides with the loss of the $(OH)^-$ groups, while in the temperature range where SO_3 is lost, measurements with a sensitivity better than 0.1 % would have to be performed in order to resolve a 100 K temperature difference. This may be surprising considering that the loss of SO_3 accounts for more mass loss than the loss of $(OH)^-$. However the subreactions making up the loss of SO_3 in the decomposition model are strictly sequential. Conversely, parallel reactions occur during the loss of the $(OH)^-$ groups.

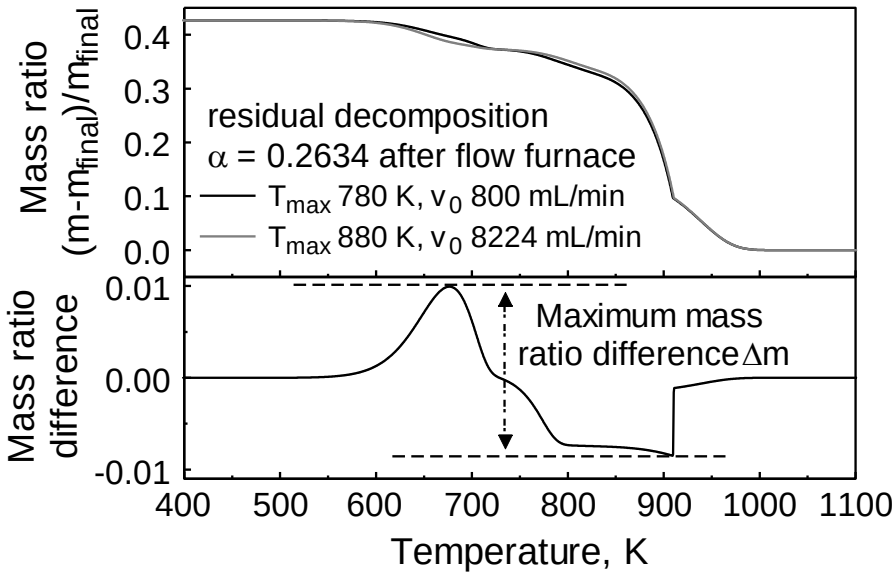

Figure 3.6 Data reduction for the purpose of systematic comparison of residual decomposition curves for different flow furnace conditions.

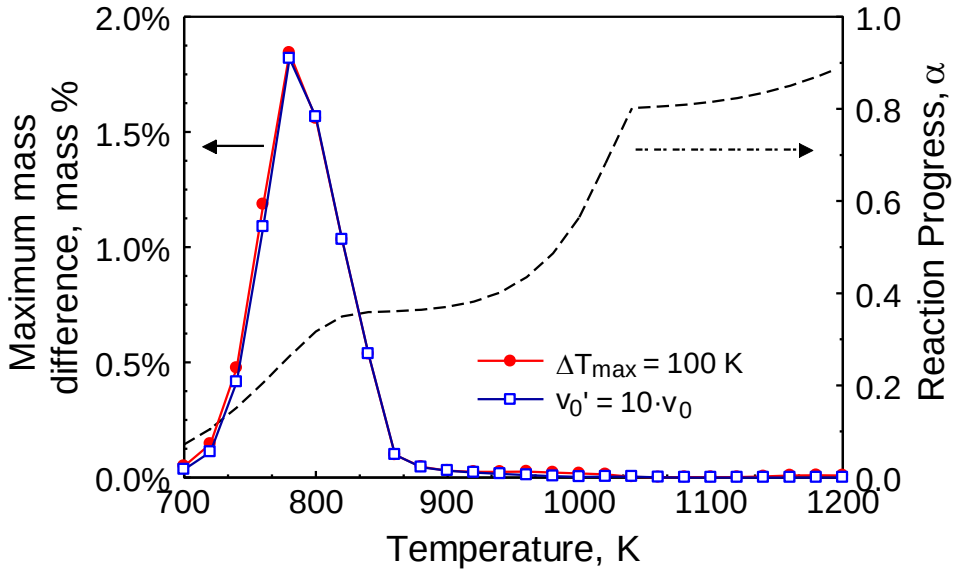

Figure 3.7 Sensitivity analysis showing the accuracy required in residual decomposition measurements to discriminate temperature differences of ΔT_{max} = 100 K (filled bullets), and a change in base flow rate v0 by a factor of 10 (open squares).

3.4 Results and Discussion

The residual decomposition from both TG experiments and model calculations are expressed as the ratio of sample mass to the mass of the completely decomposed material, $(m-m_{final})/m_{final}$, since this is the only state common to materials recovered from different temperature profiles. The results are shown in Figure 3.8. The solid lines represent the experimental data and the dashed lines represent the calculations.

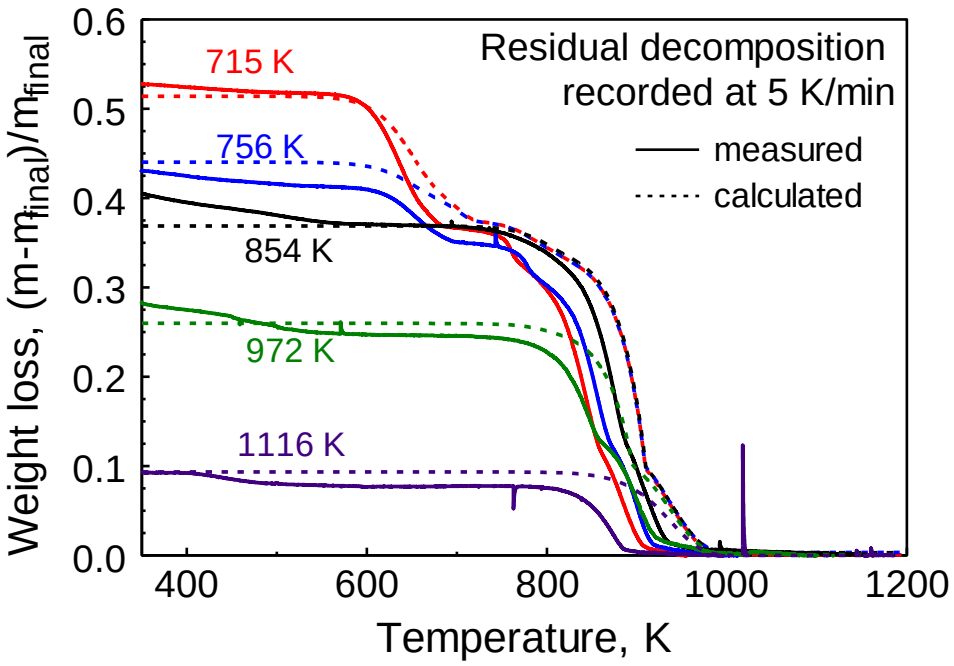

Figure 3.8 Residual decomposition of partially decomposed jarosite recovered from the flow furnace. Numbers indicate the measured maximum temperature.

For all experiments, the overall weight difference observed during residual decomposition matches the calculated value to within 5-10 %. However, the experimental curves are sufficiently noisy, and their reproducibility is relatively poor, so that details of the decomposition curves do not match very well between observations and calculations. A higher sample mass in the readout measurements would have given higher accuracy.

With this in mind, it is still useful to examine what maximum temperature and base flow rate would have been recovered from the experiments alone, and how well they would have matched the experimental conditions shown in Table 3.1. The above sensitivity analysis (see Figure 3.7) suggests that the predictive power is greatest under conditions where the $(OH)^-$ groups are partially lost. Therefore, the readout curve that

was recorded after partial decomposition with a T_{max} of 756 K and a base flow rate of 799 mL/min was treated as if the decomposition conditions were unknown.

The readout curve includes information about the actual value of α achieved by heat treatment as well as about the $T(t)$ profile the particles were exposed to. Given that the differences among readout curves are relatively small, if α is held constant (see Figure 3.6 and Figure 3.7), and that the measurements are noisy (Figure 3.8), it is expected that a set of conditions with similar α will fit the measured readout curve nearly equally well.

Decomposition and readout curves (see Figure 3.4) were calculated for maximum temperatures ranging from 650 to 900 K and for flow rates ranging from 50 to 10,000 mL/min. The computed readout curves were then compared to the experimental readout curve by calculating the sum of the squared differences between experimental and computed curves. A contour plot of the sum of square differences is shown in Figure 3.9. It shows a valley along a trend paralleling the constant α curves shown in Figure 3.5. The global minimum in this valley is found at T_{max} = 800 K and v_0 = 1450 mL/min. Comparing this to the actual experimental conditions of 756 K and 799 mL/min gives a temperature offset of 44 K and a base flow rate different by a factor of 1.8.

The result is encouraging in that the obtained values are reasonably close to the experimental conditions. More accurate results are expected if larger sample masses are available for readout measurements.

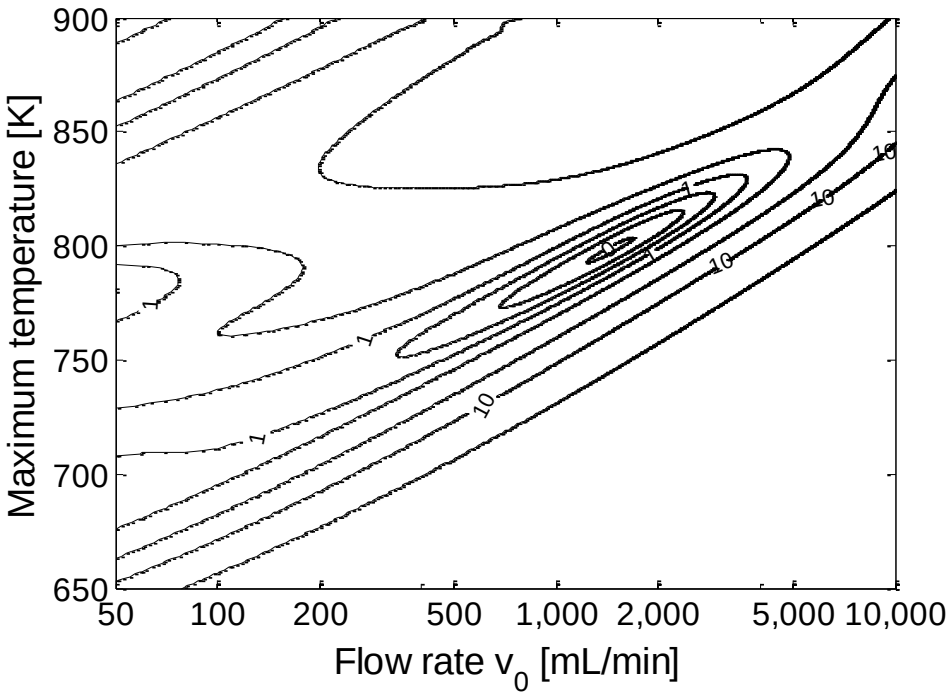

Figure 3.9 Contour plot of computed mean square differences between observed and calculate readout curves. The contour lines are logarithmically spaced to aid visibility near the minimum.

3.5 Conclusion

A conventional material, a synthetic form of the mineral K-H_3O jarosite was evaluated for use as a temperature witness material. A flow furnace experiment was designed to expose a jarosite aerosol to temperatures up to 1200 K, for times of 10 seconds and less. The jarosite particles partially decomposed during this exposure, were recovered, and the residual decomposition was determined by TG. In parallel, the partial decomposition in the flow furnace as well as the residual decomposition were calculated based on a previously published kinetic decomposition model. Experimental and calculated residual decomposition curves are in reasonable agreement. The overall mass loss matches well. Although details of the residual decomposition curves are less reproducible and their

measurement is limited by the resolution of the TG experiments, temperatures and flow rates used in the experiments are recovered well under conditions where the $(OH)^-$ groups of the jarosite are partially lost.

A sensitivity analysis of the decomposition model shows that it has the greatest power to resolve temperature and flow rate differences in the flow furnace if the temperature is near 800 K, which coincides with the loss of $(OH)^-$ groups from the jarosite structure. In this temperature region, in order to resolve a 100 K temperature difference in flow furnace conditions, the residual decomposition must be determined with a resolution better than about 1.5 wt-%. At higher temperatures, where the decomposition causes the loss of SO_3 from the jarosite structure, the resolution requirement for the residual decomposition measurements is too stringent for their practical use.

The difference in sensitivity associated with the $(OH)^-$ loss vs. the SO_3 loss suggests that if one were to search for suitable thermal witness materials or aim to design novel materials for this purpose, a set of parallel reactions are more useful regardless of the overall weight loss than a set of sequential reactions.

Application of the evaluated material to real-world combustion environments remains to be evaluated separately. Specific issues are the effect of time scales, pressure and also the concentrations of certain species in the combusting environment like oxygen, SOx etc. on the decomposition kinetics. Regarding time scales, while heating rates may be much higher than used in this study, cooling rates in the absence of adiabatic expansion are relatively slow, and total exposure times can also measure in seconds. Fidelity of the temperature history may be sacrificed for an overall, integral temperature

dose parameter. Regarding decomposition kinetics, while the decomposition of simpler materials are unquestioningly better characterized, it is essential to use complex materials with independent decomposition reactions in order to decouple time and temperature. Finally, as the kinetic models improve, pressure effects and also the interaction with the environment can more effectively be taken into account.

CHAPTER 4

RECOVERING THERMAL HISTOIRES FROM QUENCHED GLASS PARTICLES

4.1 Introduction

Specialized pyrotechnic materials and devices are being developed to achieve tunable temperature and pressure effects over short time spans [43-46]. To aid in this development, a method for accurate characterization of the produced temperature-time signatures is useful. A number of methodologies for rapid (milliseconds to seconds) high-temperature (1000 K and above) measurements exist [13, 33, 47, 48]. One such methodology relies on temperature-sensing particles, which are dispersed in the pyrotechnic event, recovered after the event, and subsequently read out to reveal the temperature history of their environment with some degree of spatial resolution.

In order to be useful as temperature sensors, materials should respond to a thermal stimulus with changes that are quantifiable in temperature and in time. This can be achieved by explicitly considering thermally activated reactions, such as thermal decomposition (see above), or diffusion and grain coarsening [13, 34]. Other sensor particles have been investigated based on a strictly temperature-dependent change in thermoluminescence [33]. Even in cases where the time component is not inherent in the temperature-sensitive process, the short time scale of the temperature exposure may provide a way to exploit particle-size-dependent heat flow characteristics in combination with the temperature response.

Glass forming liquids undergo a characteristic time- and temperature dependent process during transition to a solid. As the liquid cools, the viscosity increases, and the atomic mobility decreases, eventually resulting in the solid glass. This glass transition

generally shifts to higher temperatures as the cooling rate is increased. Different glass transition temperatures signify different atomic structures of the glass, which persist to room temperature, and can be analyzed and quantified. Therefore, the structure of the glass after cooling carries information about the cooling rate during the glass formation.

Among the structural properties that are frozen in at the glass transition is the degree of cross-linking, or polymerization of the SiO_4 tetrahedral structural units in silicate glasses [49-52]. The degree of polymerization can be characterized by quantifying the relative amounts of SiO_4 units with 0 – 4 bridging oxygen atoms by spectroscopic methods such as Raman spectroscopy, Nuclear Magnetic Resonance (NMR), Brillouin scattering and others. By developing a calibrated correlation between cooling rate at the glass transition and the Raman spectrum, details of the cooling process can be recovered.

In order to be useful as a temperature sensor, a clear relationship between atomic structure at room temperature and the cooling rate during glass formation must be known. To establish such a calibrated relationship for selected glasses, a hyperquenching experimental setup was built. Powders of soda lime glass, and of sodium silicate $Na_2O{\cdot}2SiO_2$ were subjected to melting, rapidly quenched, and subsequently analyzed by Raman spectroscopy. In addition to a previously developed heat transfer model, a numerical simulation was used to define the relation between particle temperature and the environment temperature. A methodology to recover temperature-time profiles during exposure is developed.

4.2 Methodology to Recover Thermal Information

Consider glass particles inserted into a hypothetical temperature profile with a heating branch, a maximum temperature, and a cooling branch. As the particles are heated, they first undergo the glass transition and eventually pass the thermodynamic melting point. When such particles are heated above the glass transition (but below melting), the degree of linking, or polymerization, in the SiO_4 network decreases with increasing temperature. Upon cooling the process reverses: the network forming SiO_4 units begin to polymerize until the glass transition is reached. At this point, no further polymerization occurs with further temperature decrease – the degree of SiO_4 unit linking, or polymerization is frozen-in. However, the glass transition temperature is a function of the cooling rate [59]. Therefore the structure that is frozen in at the glass transition depends on the cooling rate as well. The following section describes how this effect can be used to recover practically relevant temperature-time profiles from particles exposed to unknown, but rapidly changing high temperatures.

As the environment around the aerosolized particles cools, particles with different sizes will experience size-dependent thermal lag. The following simple analysis shows how cooling rate, particle and environment temperature are related under continuum heat transfer conditions. Heat flow from a hot glass particle cooled in air is described as:

$$\dot{Q}_p = \rho V_p C_P \frac{dT_p}{dt} = A_p \frac{\lambda(T) Nu}{2r_p}\left(T_e - T_p\right) \tag{4.1}$$

where $\dot{Q}_p$ is the heat flow from the particle to the environment, T_p and T_e are particle and environment temperatures, respectively; V_p, A_p, r_p, C_p, and ρ are respectively

the particles' volume, surface area, radius, heat capacity, and density; Nu is the Nusselt number, and λ(T) is the temperature-dependent thermal conductivity of air. Consider cooling when the particle temperature T_p corresponds to the glass transition temperature T_g. Once the particle cooling rate has been recovered (e.g., by Raman spectroscopy), and the size of the particle is known from microscopy, this Equation can be solved for the environment temperature directly. From a set of particles of different sizes, one can therefore obtain a set of environment temperatures:

$$T_e = T_g + \frac{\rho V_p C_P}{A_p} \frac{dT_p}{dt} \frac{2r_p}{\lambda(T) Nu} \tag{4.2}$$

This is not sufficient to construct a time-dependent temperature profile. One must also recover information about the time component. Simple differentiation of Equation (4.2):

$$\frac{dT_e}{dt} = \frac{dT_p}{dt} + \frac{\rho V_p C_P}{A_p} \frac{d^2T_p}{dt^2} \frac{2r_p}{\lambda(T) Nu} \tag{4.3}$$

shows that the cooling rate of the environment at T_e is equal to the cooling rate of the particle at T_g plus a correction that is proportional to the second time derivative of the particle temperature. If this second derivative were known, the actual cooling profile could now be recovered from the set of (T_e, dT_e/dt) values – either by treating these values as boundary conditions to a differential Equation, or graphically by plotting T_e vs. dT_e/dt and comparing the trend to a model, such as exponential cooling.

The second derivative of the particle temperature is however not known a priori. One could assume that it is zero, and accept an error that is proportional to $1/\tau^2$ where τ is the time constant in the case of an exponential cooling function. One can also approximate the actual dT_e/dt iteratively with the following steps: (1) assume $dT_e/dt = dTp/dt + \Delta$ with $\Delta=0$ initially, (2) recover $T_e(t)$, e.g., graphically, (3) perform a model calculation of how particles would cool in this environment, (4) determine the second time derivative of the particle temperature, and (5) calculate an estimate for Δ and use it to start over with step (1). This sequence can be repeated until the values for Δ converge.

The principal requirement for this scheme to recover environmental cooling profiles is the ability to determine the cooling rate that a given particle has experienced. Analysis of the Raman signals, as discussed in this chapter, might provide this ability. Therefore it becomes possible in principle to recover an accurate $T_e(t)$ profile from the analysis of exposed glass particles. The concept is summarized in Figure 4.1.

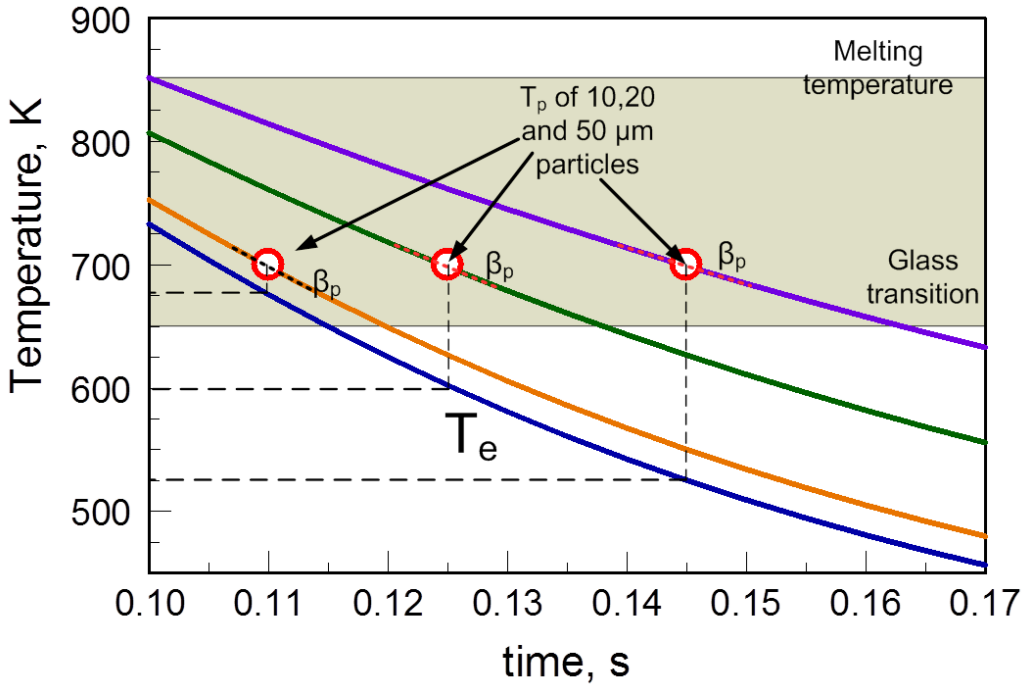

Figure 4.1 Schematic plot showing different size particles cooling with the environment to illustrate the concept of temperature recovery. Particle cooling rates are shown as β_p.

Temperature profiles, as illustrated in Figure 4.1, can only recover environmental temperatures up to the glass transition of the glass that is being used. Higher temperatures cannot be recovered from the above analysis, and additional observations must be used. Such information may be available experimentally, if one can determine the largest particle size that experienced proper melting, as recognized by the change of particle shape. If the original glass particles have irregular shapes, they will become spherical once the thermodynamic melting point is reached. Under shock conditions shapes may be deformed, but the change from the original shape should be readily recognizable. In a population of particles with a wide size distribution, smaller particles will reach high temperatures first, and one expects that only the largest particles remain un-molten. To melt a particle, certain energy needs to be transferred to it, determined by

the particle heat capacity. This energy could have been imparted to the particle by exposure to high temperatures for a short time, or to lower temperatures for a longer time. In general, the *T(t)* curve describing the energy required for particle melting will be asymptotic with the temperature axis at $t=0$, and with the time axis at $T=T_m$. where T_m is the thermodynamic melting point of the glass.

It is useful to consider the maximum environment temperature as a point on the *T(t)* curve. One can then use a second glass with a different composition – which may be easily recognized by its different Raman signature – which would have a different T_m and characteristic *T(t)* curve that describes the energy required to melt the largest molten particle recovered. One point in the $T_e(t)$ profile of the actual environment temperature would then be the intersection of the two particle T(t) curves. This concept is illustrated schematically in Figure 4.2.

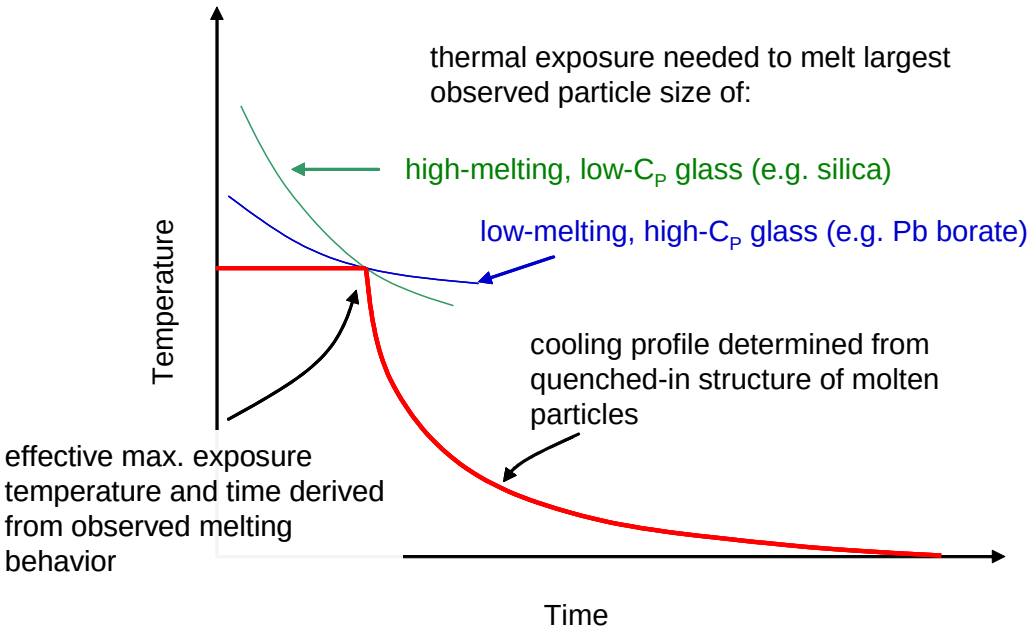

Figure 4.2 Schematic plot illustrating the concept of recovering maximum temperature.

This procedure is not able to recover any detail before the onset of cooling, and a constant temperature with certain duration must be assumed. This is not necessarily a drawback in the context of the present research: for any given material exposed to the environment temperature it is more important how much energy has been transferred to it from the environment rather than what the exact *T(t)* profile was.

4.3 Experimental Section

4.3.1 Material

Two different glasses were exposed to rapid cooling conditions to determine whether different cooling rates can be distinguished, and to establish respective quantitative relations with a suitably chosen indicator.

Commercial soda-lime glass in the form of microscopy slides (Premiere microscope slides, estimated composition: SiO_2 73 wt-%, Na_2O 14 wt-%, CaO 9 wt-%, MgO 4 wt-%) was ground using a mortar and pestle and size classified. Particles with sizes less than 53 µm were used for rapid exposure tests.

Sodium silicate glass $Na_2O{\cdot}2SiO_2$ (NS_2) was synthesized in a two-step procedure. A 8.66 gram batch of NS_2 was prepared by mixing appropriate amounts of laboratory grade sodium metasilicate ($Na_2O.SiO_2$) from Sigma Aldrich and laboratory grade fumed Silicon(IV) Oxide (99.8%) from Alfa Aesar. The mixture was mixed using a Spex Certiprep 8000 series high energy shaker mill with 5 zirconia balls in a zirconia vial. The mixed sample was then pressed into ¼ inch pellets and calcined at 600 °C in a furnace for 12 hours. The resulting mixture was then melted in a graphite crucible in a furnace at

1200 °C for 5 minutes, and poured on to a graphite slab. After cooling the glass was crushed with a mortar and pestle, and remelted to improve homogeneity. Eventually, the glass was crushed and sieved using a 270 mesh to obtain particles <53 μm.

4.3.2 Characterization

SEM images were taken using a Phenom Tabletop Microscope by FEI Technologies Inc. Raman spectroscopy was performed using a Thermo Scientific DXR confocal Raman Microscope. A 532-nm excitation laser with 50-μm aperture was used. 10X and 50X objectives were used to identify and analyze glass particles. The Raman spectra were processed using the Thermo Scientific OMNIC 8.1 Series data collection, visualization, processing and analysis tool.

Glass transition temperatures were determined using a Netsch STA409 PC differential scanning calorimeter. Approximately 10 mg of glass was placed in a Pt crucible, cooled at various rates, and reheated to obtain the fictive temperature, defined as the temperature at which the liquid structure is frozen when cooling down through the glass transition.

4.3.3 Thermal Exposure Experiments

The relation between structural properties of the glass and cooling rate at the fictive temperature/glass transition should hold over a wide range of cooling rates. Therefore, the glass was exposed to cooling rates on the order of K/min as well as to higher cooling rates, above 100 K/s. The slow cooling experiments were performed using a Netzsch Simultaneous Thermal Analyzer STA409 PC Differential Scanning Calorimetry (DSC) in mixed argon (Matheson Tri-Gas, 99.999%) and air (Airgas, zero grade) environment.

Sample masses were 20-30 mg. The glass was placed on an alumina crucible lid, heated to ~700 °C, and then cooled at a controlled rate selected in the range of 1 – 40 K/min. The samples typically fused into a large droplet, but did not spread significantly across the sample support.

In order to achieve higher cooling rates, a custom experiment was designed where aerosolized particles pass from a high-temperature environment through a choked-flow nozzle into a low-pressure environment, where the surrounding gas is cooled by adiabatic expansion and further, by exposure to colder surroundings. The experimental setup is illustrated in Figure 4.3. It consists of a vertically mounted 1" ID alumina furnace tube, which is heated by a coil of 17 gauge Kanthal wire (KA1, Hyndman). The heater is powered by a variac, allowing one to adjust the working upstream temperature. At the lower end of the heated segment, a 375-μm orifice is mounted on a 0.5" OD 22 cm long mullite collection tube. The mullite tube was attached to a 75 cm long steel tube using a Cajon® feedthrough fitting. The orifice was prepared by solidifying zirconia cement (904 Zirconia Ultra High Temperature Ceramic Adhesive, Cortronics Corp. NY) around a vertically aligned nylon monofilament of 0.375 μm diameter, and subsequently burning out the filament. At the bottom end of the collection tube, a small piece of aluminum foil is mounted on a coarse grid, allowing particles to settle onto the foil, while gas passes through the grid to a rotary vacuum pump. This collection foil is placed 72 cm away from the nozzle as shown in Figure 4.3. A static pressure transducer (PX209-30VAC5V, Omegadyne, Inc.) is used to measure the pressure in the low-pressure downstream section, and a bypass valve can be used to adjust the downstream pressure. The space

between furnace and collection tubes is filled with thermal insulation in order to minimize convection.

The actively heated segment of the furnace tube is 10 cm in length, selected based on an estimate of the time required to heat a ~50 µm glass particle to its melting temperature while taking into consideration a maximum furnace temperature of 1450 K, the density, thermal conductivity and the melting point of the glass, and the particle settling velocity.

Particles are introduced using a vibratory feeder at the top of the furnace. Perfect aerosolization is not required, as quenched particles are analyzed by optical microscopy, allowing one to distinguish individual particles. Using irregular-shaped glass particles makes it possible to determine whether the time a particle spent in the high-temperature upstream section was long enough to melt the particle.

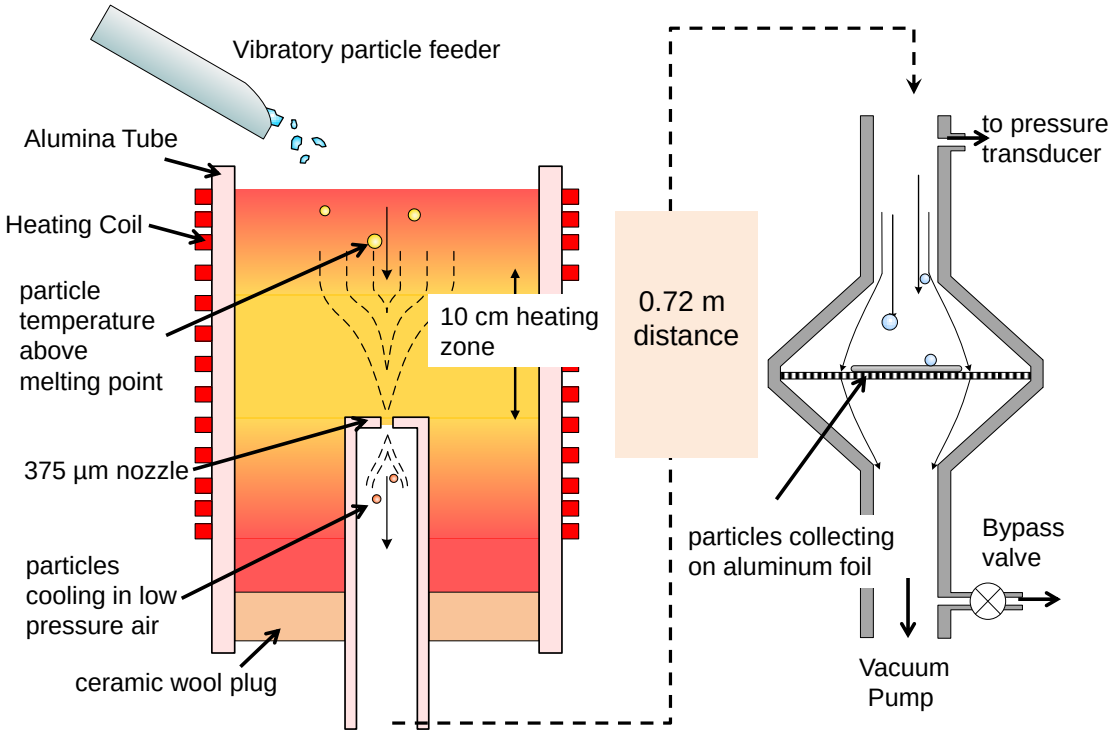

Figure 4.3 High-quench rate particle exposure experimental setup.

A K-type thermocouple from Omegadyne, Inc was used to measure the axial temperature in the tube furnace, the thermocouple was allowed to equilibrate for 30 minutes at each position in the heated segment prior to recording. A measured temperature distribution in the heated segment of the tube furnace for a typical, 90-V, variac voltage is shown in Figure 4.4. The measured temperature distribution in the heated segment is stable and reproducible. The maximum temperatures in the heated segment for different input voltages are shown in Figure 4.5. Similarly, temperature measurements using the thermocouple were performed in the downstream section at 0.03, 0.07 and 0.09 atm pressures at various axial locations as shown in Figure 4.6. The variation of the axial temperature in the steel section is comparable for all the pressures; hence this section can be described by an exponential fit that is universal for all the operating pressures. The black curve in Figure 4.6 represents the temperature fit.

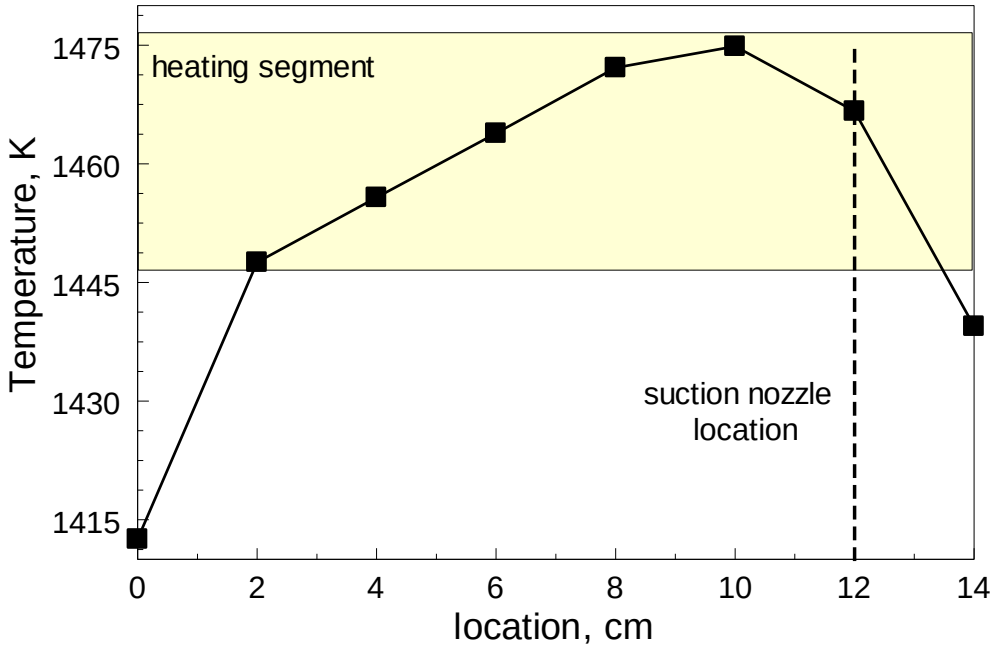

Figure 4.4 Temperature in the heated segment.

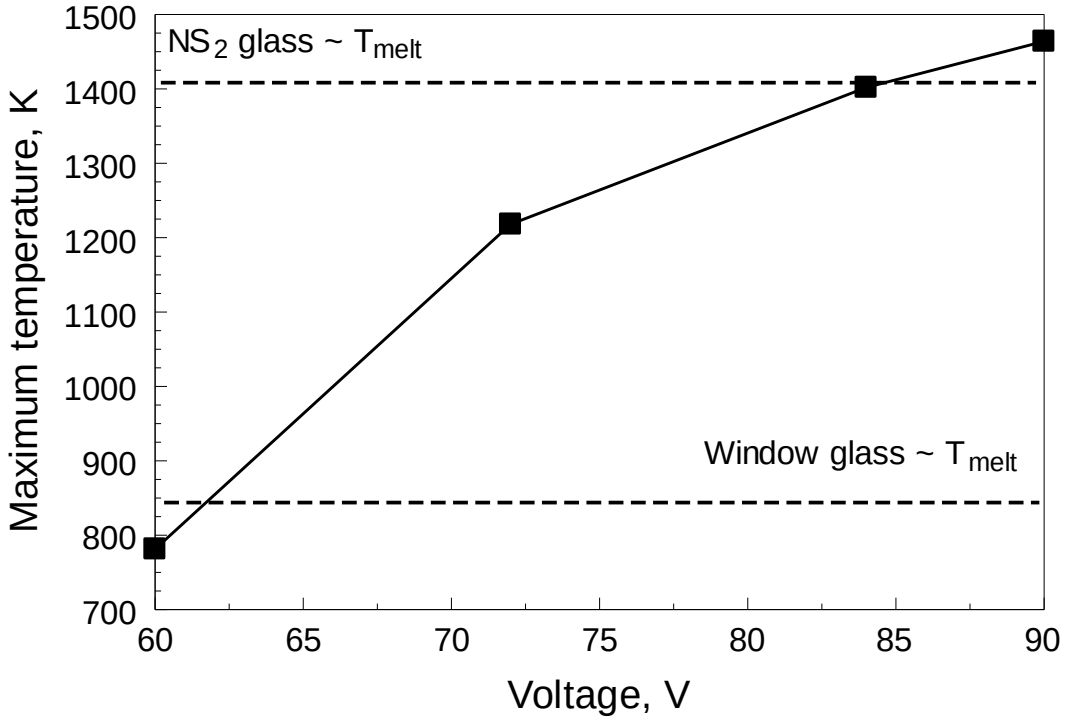

Figure 4.5 Maximum temperature in the heated segment vs. voltage settings.

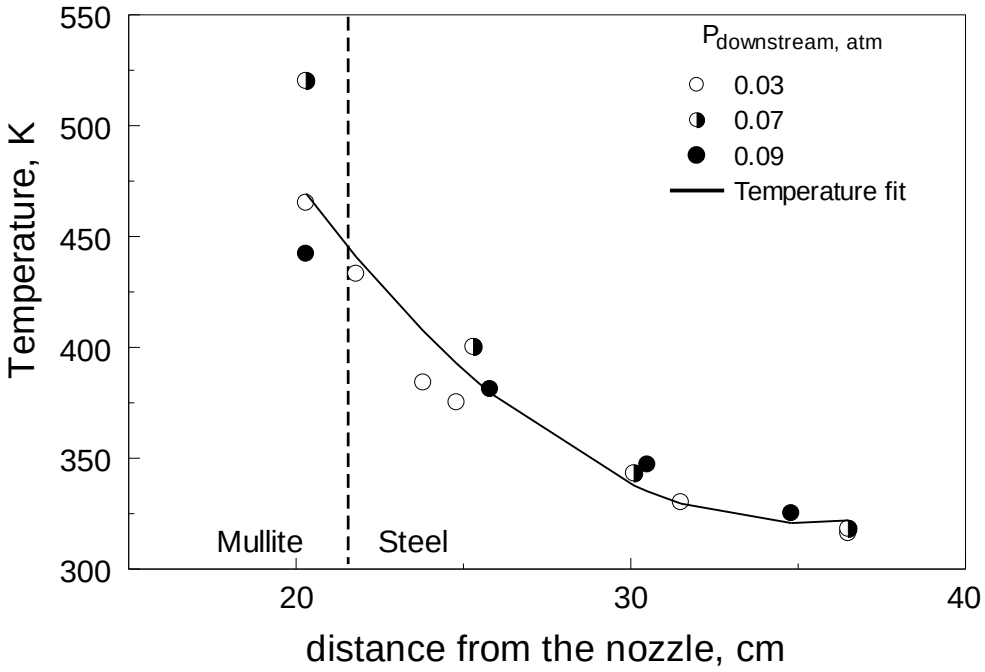

Figure 4.6 Thermocouple temperature measurements downstream from the nozzle.

A wide range of operating temperatures is available to test glasses with different melting and glass transition temperatures. The list of experiments performed for both window glass and NS_2 glass are tabulated in Table 4.1.

Table 4.1 List of Experiments Performed

Type of Glass	Upstream Temperature, K	Downstream Pressure, atm
Window Glass	1475	0.034
Window Glass	1475	0.15
NS_2 Glass	1400	0.02
NS_2 Glass	1400	0.023
NS_2 Glass	1400	0.03
NS_2 Glass	1400	0.06
NS_2 Glass	1400	0.09
NS_2 Glass	1460	0.06

4.3.4 Experimental Determination of Glass Transition Temperature

Slow cooling experiments were performed to determine the fictive temperature (T_f) at various cooling rates by using a Netzsch Simultaneous Thermal Analyzer STA409 PC Differential Scanning Calorimetry (DSC) in mixed argon (Matheson Tri-Gas, 99.999%) and air (Airgas, zero grade) environment. Sample masses were 20-30 mg. The glasses were placed on a platinum pan, heated to 900 °C, and then cooled at different cooling rates; the glass was subsequently heated after each cooling experiment to determine the fictive temperature (T_f).

The fictive temperature was determined by following the standard procedure recommended by DIN 51007E *via* the Netzsch Proteus 6® software. Figure 4.7 shows the heat flow recorded at 10 K/min from a NS2 sample that had been previously cooled at 60

K/min. The fictive temperature is taken as the temperature T_f, at which the following Equation is satisfied [59]:

$$\int_{T_1}^{T_2} (C - C_{glass})dT = \int_{T_f}^{T_2} (C_{liq} - C_{glass})dT_f \tag{4.4}$$

Here, C is the measured heat capacity, C_{glass}, is the extrapolated heat capacity of the glassy solid below the glass transition, while C_{liq} is the heat capacity of the supercooled liquid above the glass transition. This is illustrated in Figure 4.7

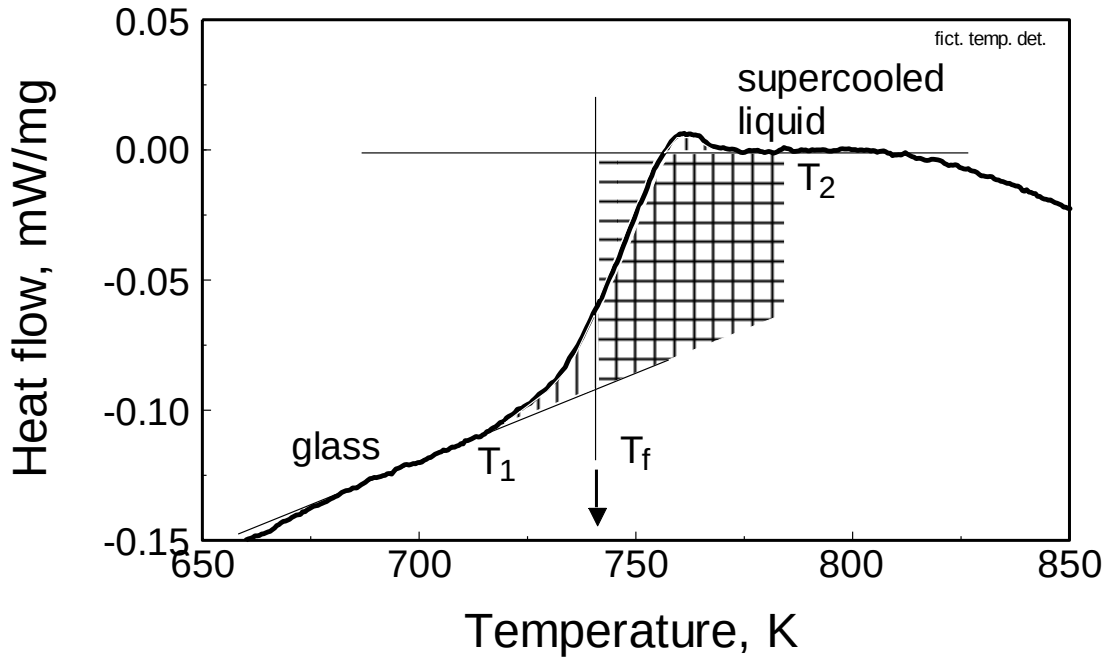

Figure 4.7 Determination of Fictive Temperature (T_f) for a NS_2 glass that was previously cooled at 60 K/min.

The fictive temperature shows an Arrhenius-like dependence on cooling rate [59]:

$$\ln\left(\frac{dT}{dt}\right) = -\frac{E_A}{R}\frac{1}{T_f} + C \tag{4.5}$$

characterized by an activation energy E_A, and a pre-exponential constant C. Figure 4.8 shows the inverse fictive temperature for the glasses used here as a function of the cooling rate on a logarithmic scale. The slope for NS2 corresponds to an activation energy of 878±250 kJ/mol, implying a change of tens of K as the cooling rate is increased 2-3 orders of magnitude. For soda lime glass, the change of T_f with cooling rate is too small to measure, and an average value of 846.6 K will be used.

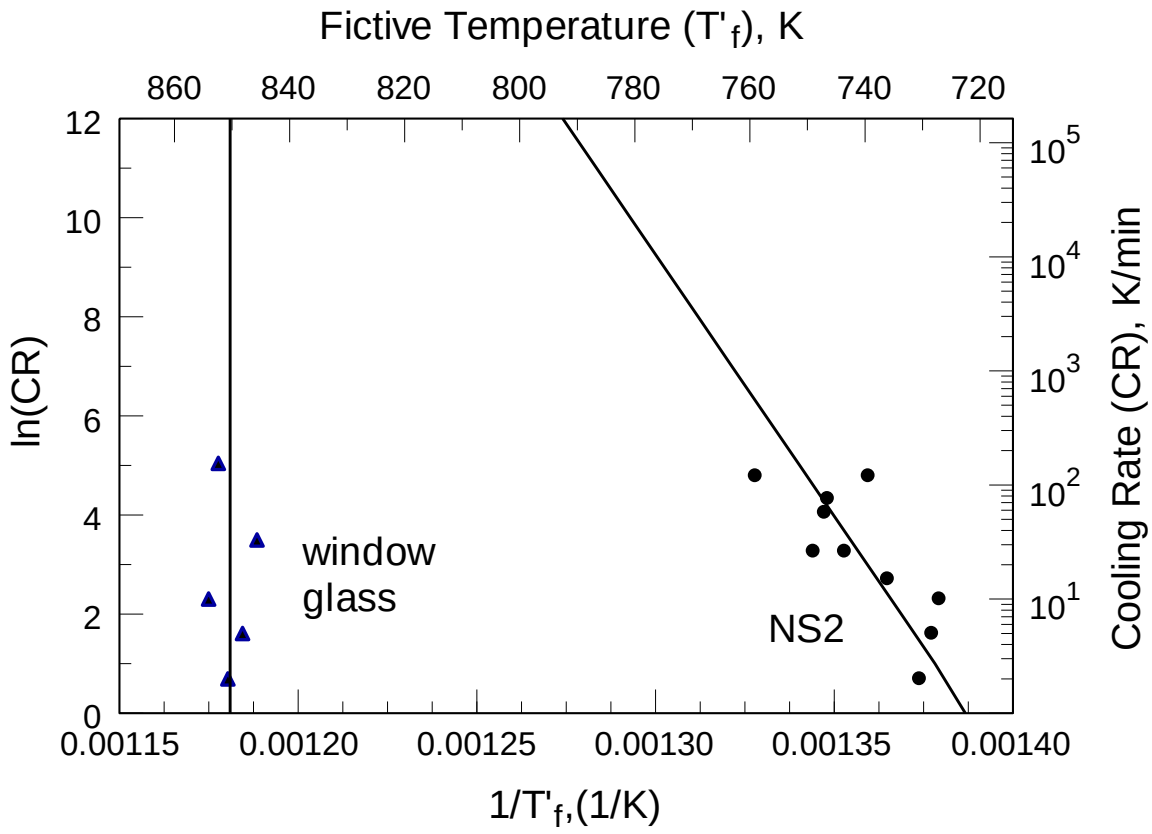

Figure 4.8 Fictive temperature as function of cooling rate for NS2 and soda lime glass.

4.4 Axisymmetric 2D Simulations

4.4.1 Simulation Setup

Ansys Fluent 15 was used to simulate the compressible flow established in the experimental setup and assess cooling rates of particles experiencing different trajectories in the flow.

4.4.2 Geometry

Simulation of the entire experimental setup (see Figure 4.3) is time and resource intensive. A simpler and more practical approach is to model the region where glass particles quench, i.e., the collection setup (see Figure 4.3). The downstream temperature measurements shown in Figure 4.6 clearly indicate that for different downstream pressures, the gas temperatures reach ~322 K (~50 ˚C) by 35 cm. As a result, modeling the entire collection tube (22 cm mullite section and 75 cm steel section i.e. a total 97 cm section) is not necessary. A section consisting of 22 cm mullite region and 20 cm steel region was simulated as shown in Figure 4.9. A 2D axisymmetric model was chosen to limit computation time.

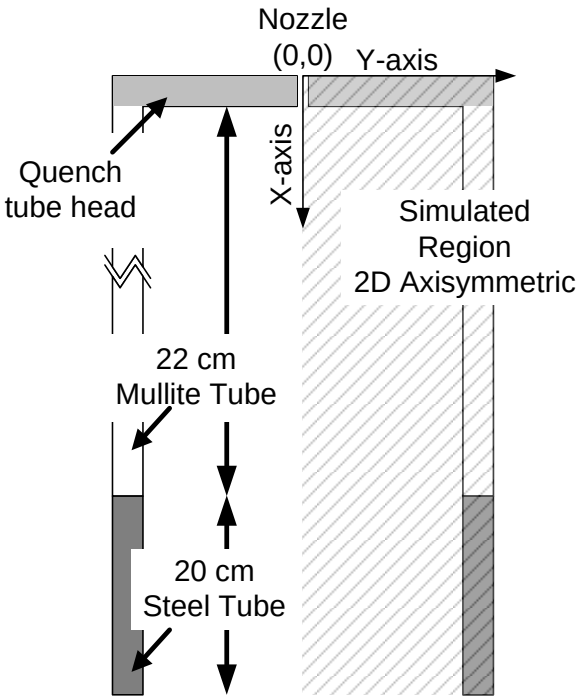

Figure 4.9 Experimental setup described in the simulation.

4.4.3 Meshing

Using an appropriate mesh and meshing method, are critical to obtaining reliable and accurate simulation results. Use of fine mesh will improve the quality of simulation, but use of only fine mesh will result to large number of cells which intern increases computational time and resources. A balance between the cell size and number of cells is needed to efficiently simulate the experimental condition.

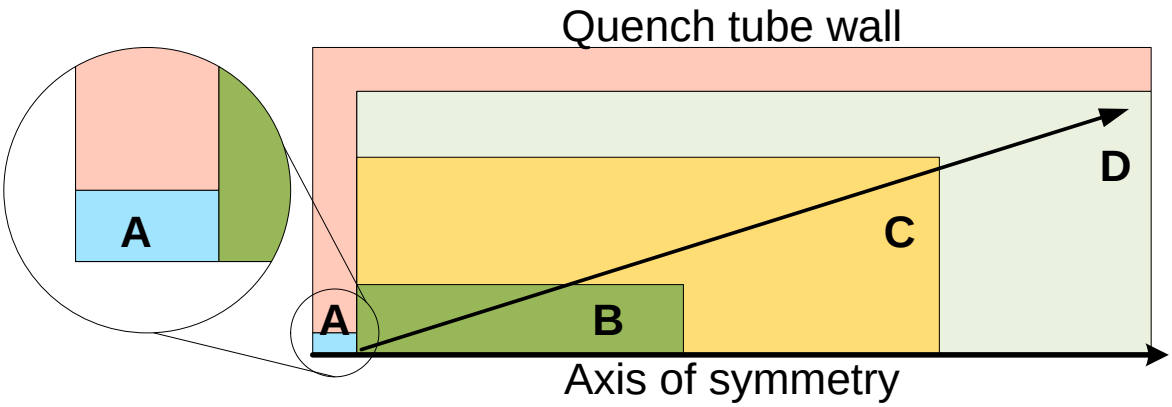

Figure 4.10 Methodology of meshing. Mesh densities decrease from region A to region D.

Figure 4.10 represents the approach used in generating the mesh used in the simulation. Quadrilateral meshes were used, the mesh density decreased from region A to region D. The densest region "A" represents the nozzle where the flow stream is developed; subsequently region "B" represents the region of adiabatic gas expansion. The dimensions of region "B" was determined by trial and error. The ratio of mesh densities were determined by factoring in the orthogonal quality (0 representing the worst and 1 representing the best quality cells) of the generated cells and the skewness factor [1 representing most skewed and <0.5 represents good quality [60]. Mesh density ratios that developed artifacts during simulations were discarded, and final ratios were deduced from successful solutions.

4.4.4 Models

Simulations were performed using a density based solver with a standard realizable k-ε model [60]. Standard thermophysical properties of air and steel where available from Fluent's material database, whereas the properties for mullite were obtained from the NIST Chemistry Webbook [61].

4.4.5 Boundary Condition

For the purpose of simplification, the exterior of the mullite tube, that was heat insulated inside the furnace, was considered as adiabatic. The quench tube head containing the nozzle was set to the upstream gas temperature shown in Table 4.1. The pressure inlet was set to 1 atmosphere and the inlet gas temperature and downstream pressure set to appropriate values based on the operating condition modeled. The temperature distribution in the mullite was obtained as a result of calculations.

The steel tube section was discretized into five parts; each of the 4 cm wall sections was assumed to have a constant temperature. The temperatures were chosen to follow the general temperature-vs-distance relation shown in Figure 4.6.

4.4.6 Simulation Results

Simulations were performed to estimate the downstream environment conditions. The flow profiles and the temperature contours were calculated for a steady state simulation. The objective of these calculations was to predict the environment temperature histories experienced by the glass particles in the quench tube. These profiles provide the information needed to calculate the particle temperature and its cooling rate.

Figure 4.11 describes the temperature profile at various radial locations along the axis of simulation. The case considered here has an upstream temperature of 1400 K and a downstream pressure of 0.09 atmospheres. The curve with Y-position 0 represents the axial temperature position. The temperature drop seen around 3-mm X-position represents the temperature drop associated with the adiabatic expansion of the gas. Bases on the operating conditions, all experiments were performed under choked flow conditions; as a result, the setup simulation captures this expected phenomenon. This

feature is shown clearly by plotting contours of temperature as shown in Figure 4.12. The radial temperature profile at various X-positions tends to converge downstream. The step-like features seen for the wall temperature profile in the steel section, represent the assumed boundary condition for the steel wall temperature (based on the downstream temperature measurement shown in Figure 4.7 and added as a dashed red curve in Figure 4.11). These superficial step features propagate into the low-temperature portions of the calculated gas temperature profiles.

Results show that the adiabatic expansion results in a short-term cooling of a small fraction of the gas. Instead, major and sustained temperature decrease occurs further downstream, in the fraction of gas exposed to the colder walls, cooled by exposure to the room-temperature environment. Respectively, the solidification of and glass transition in the glass particles is expected to occur in that portion of the expanded gas flow.

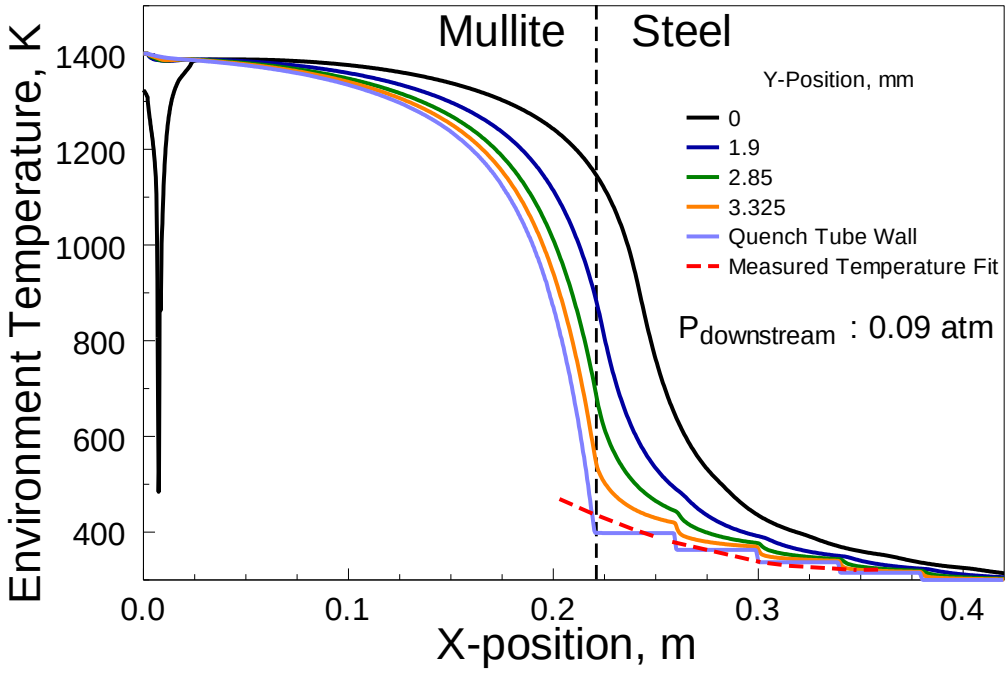

Figure 4.11 Temperature profile at various radial location along the axis of simulation.

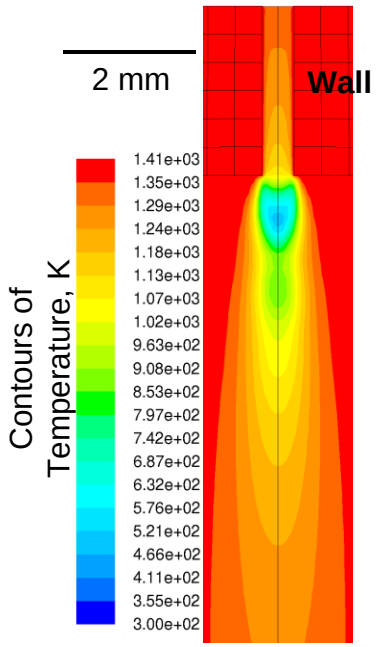

Figure 4.12 Contours of temperature around the nozzle.

4.4.7 Particle Cooling

The objective of these simulations was to observe the trajectories of the glass particles as they enter the quench tube and obtain the temperature profiles that they witness as they pass along the tube. This was accomplished in the simulation by injecting glass particles of different size at the inlet and tracking their positions and the environment properties as they travel through the quench tube.

Five glass particles spaced radially 45 μm from each other were injected at the inlet simultaneously, this procedure was repeated for different size particles. Figure 4.13 shows the particles' radial position as a function of flight time for 10 and 50 μm particles injected in a 0.09 atm downstream pressure environment. 10-μm particles pass through the nozzle and follow the flow stream of the gas, as indicated by the insert in Figure 4.13 showing an initial 5 ms window. Conversely, 50-μm particles are accelerated in the

nozzle, and less affected by the downstream, low-pressure gas flow than the smaller particles. This has the consequence that the overall residence time in the quench tube is shorter than for smaller particles, and that some particles entering off-center will touch the tube wall. In general, the degree of deflection increased with increase in particle size and downstream pressure. Particle that touch the wall while still molten are expected to stick to the wall, and to be eliminated from the result. Particles that touch the wall after they have cooled below their respective glass transition, would experience a low-temperature environment, and remain unchanged. Particles near the glass transition may, however, show unpredictable behavior.

Minor trajectory changes (maxima in Y-position) visible for the 10 μm particles in Figure 4.13 occur in the vicinity of the mullite-steel tube connection, where the boundary temperature for the gas are affected by the imposed steel wall temperature profile. This phenomenon is an artefact of the used computational scheme and decreases in magnitude as the particle size increases and the downstream pressure decrease. This effect does not alter the cooling history appreciably and is ignored in further discussion.

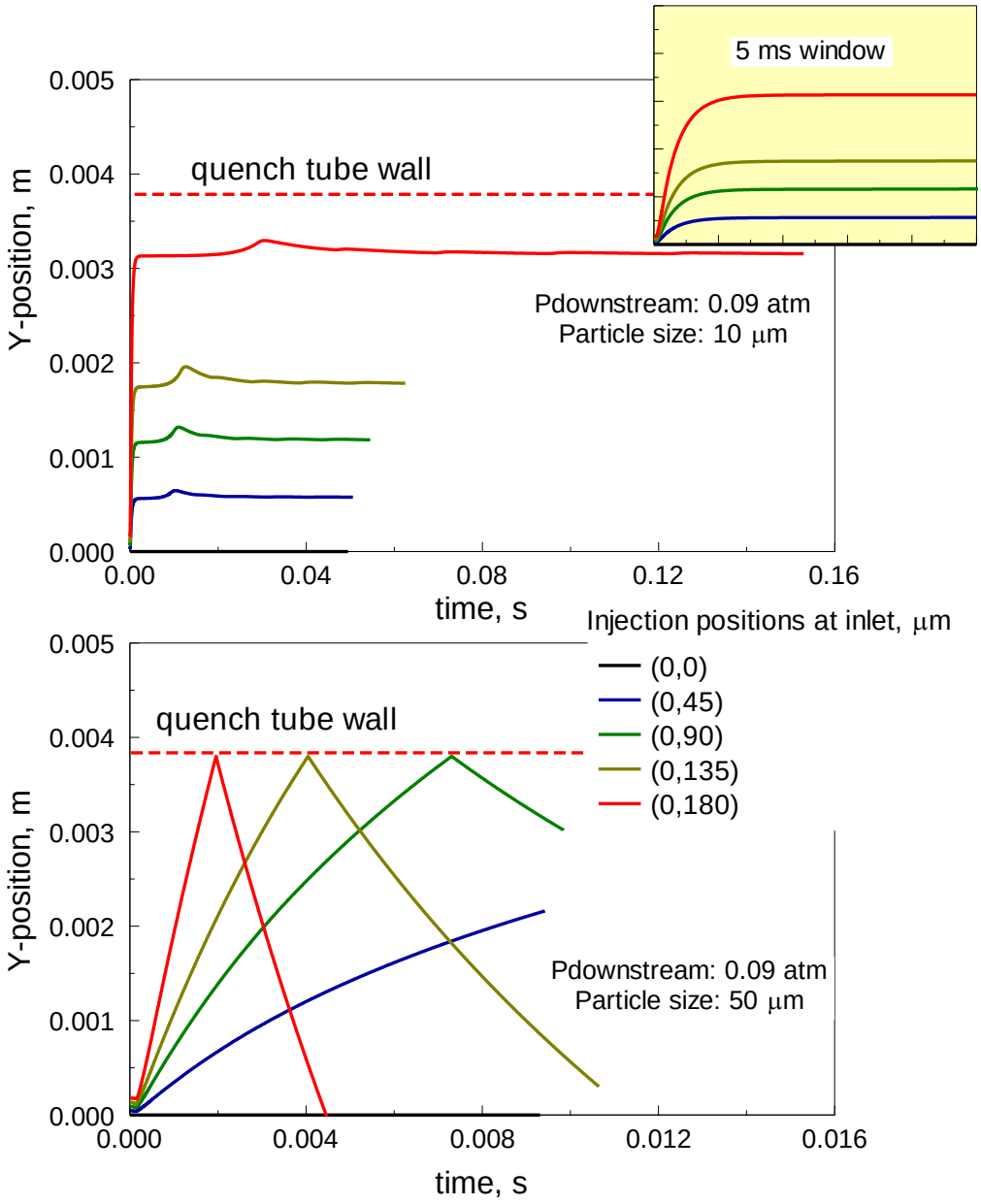

Figure 4.13 Particle trajectories for 10 μm and 50 μm particles injected in a 0.09 atm downstream pressure. The injection positions show X and Y coordinates.

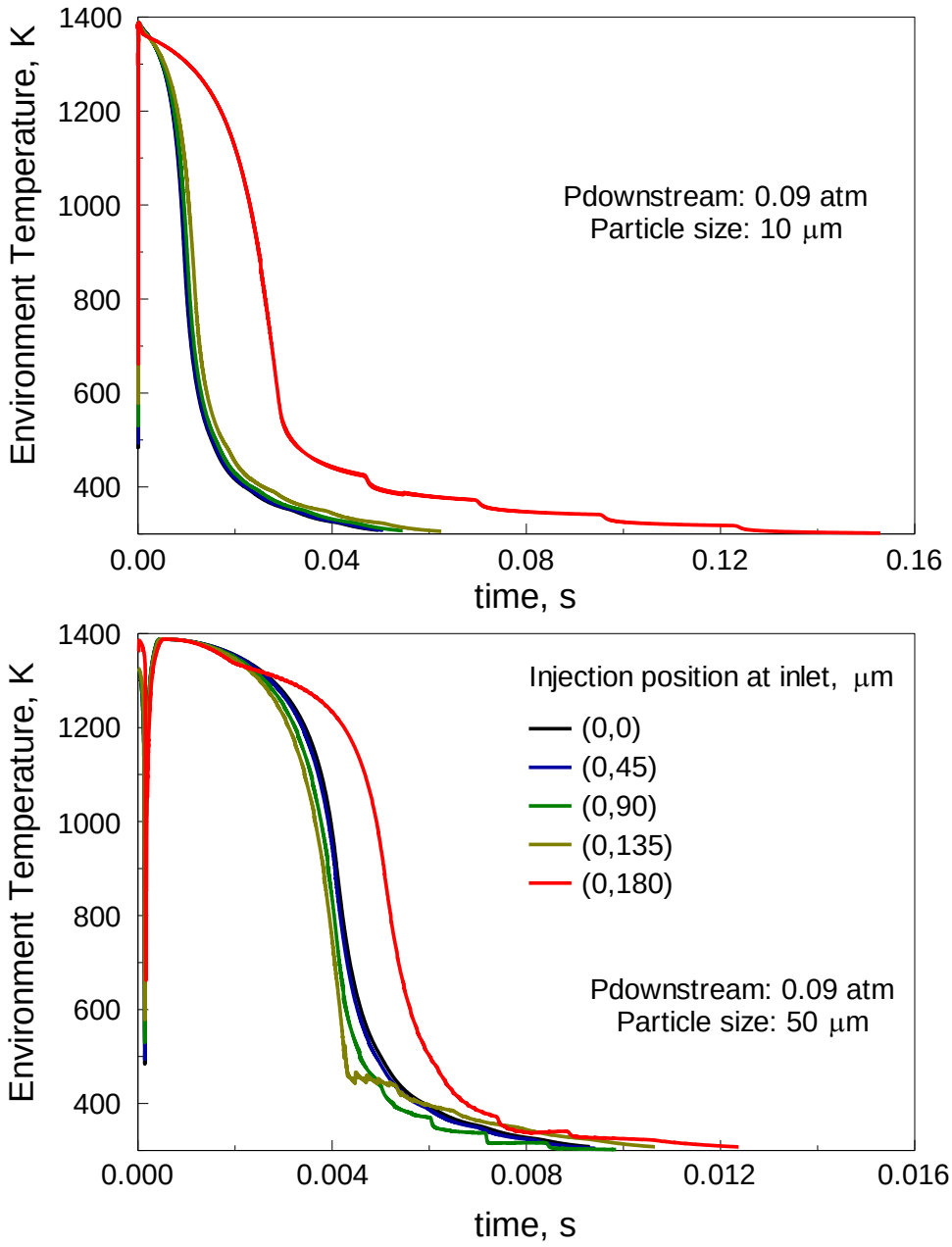

Figure 4.14 Environment temperature witnessed by the 10-μm and 50-μm glass particles injected in hot air expanding at 0.09 atm downstream of the nozzle. The injection positions show X and Y coordinates.

Figure 4.14 shows the environmental temperature the particles witness as they travel through the setup. The plots clearly indicate particles have very short residence time in the adiabatically expanding gas. Given the environment temperature, the particle

temperatures were estimated using the transition regime heat transfer model [38]. The environment and the calculated particle temperatures for 10-µm and 50-µm particles injected at (0,0) are shown in Figure 4.15. The 10-µm particle temperature follows the gas environment temperature closely; the temperature lag between the particle and the environment is small for the 10-µm particle when compared to that for the 50-µm particle. Both particles arrive at their fictive temperatures in the steel tube section (see Figure 4.11). All size glass particles injected in various downstream pressures arrive at their fictive temperatures in the steel tube section.

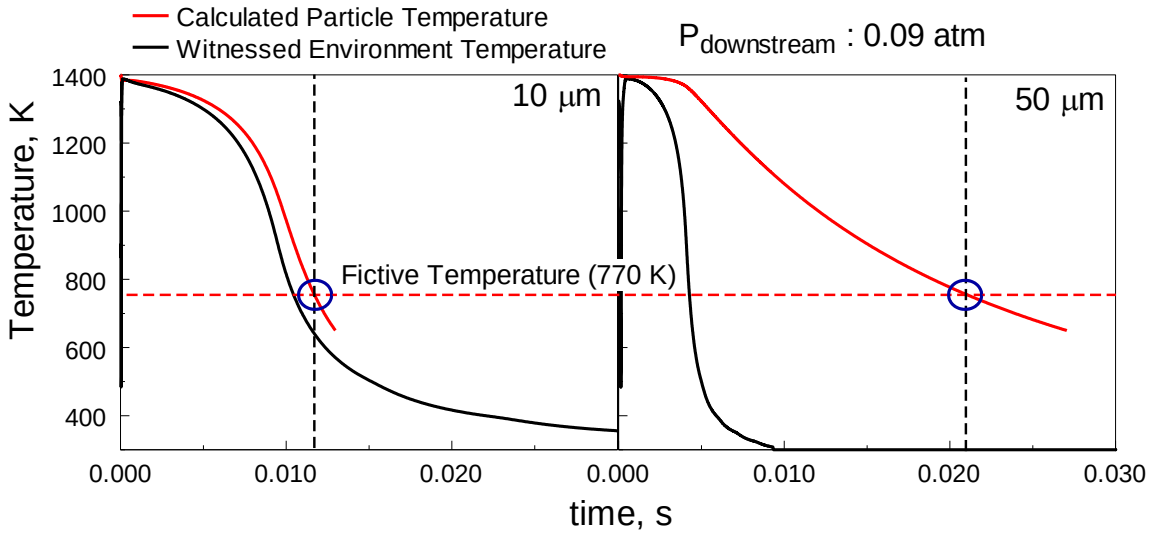

Figure 4.15 Calculated particle temperatures for 10-µm and 50-µm particles with downstream pressure of 0.09 atm.

Eliminating particles that interact with the wall, the effect of radial position with respect to particle cooling rate was investigated by calculating the particle temperature using the transition regime heat transfer model of 50-µm particles at (X,Y) positions (0,0) and (0,45µm) for the downstream pressure of 0.09 atm. Results for the temperature range close to the expected fictive temperature of NS2 glass are shown in Figure 4.16.

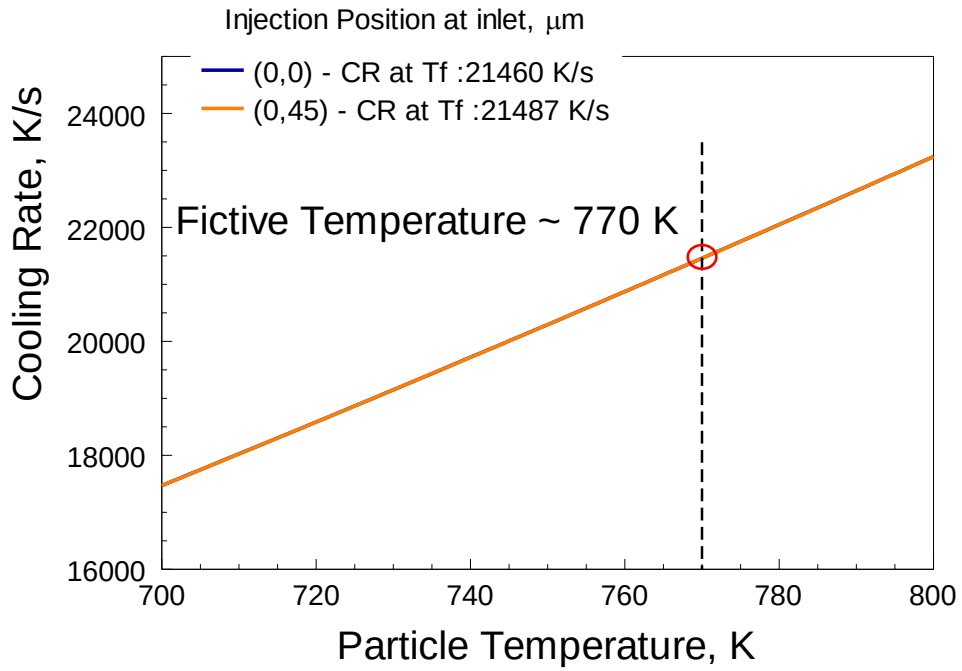

Figure 4.16 Calculated particle cooling rate for 50 μm particles injected at different positions into a 0.09 atm downstream environment.

The cooling rate curves for both initial particle positions coincide nearly perfectly, as seen in Figure 4.16**.** This clearly indicates that the cooling rate variation based on different radial positions are minimal for 50 μm particles. A similar cooling behavior was observed for different size particles at different downstream pressures. As a result, the radial temperature profile of the quench tube has a relatively small effect on the cooling rate of the glass particles near their respective fictive temperature. With that consideration, cooling rates of glass particles of various sizes starting at position (0,0) was calculated. The results are shown in Figure 4.17 for NS2 glass, and Figure 4.18 for soda lime glass. The trends of cooling rate vs. particle size are all monotonous for NS2, while a maximum, and overall very little change is observed for higher downstream pressures at the relatively higher fictive temperature of the soda lime glass.

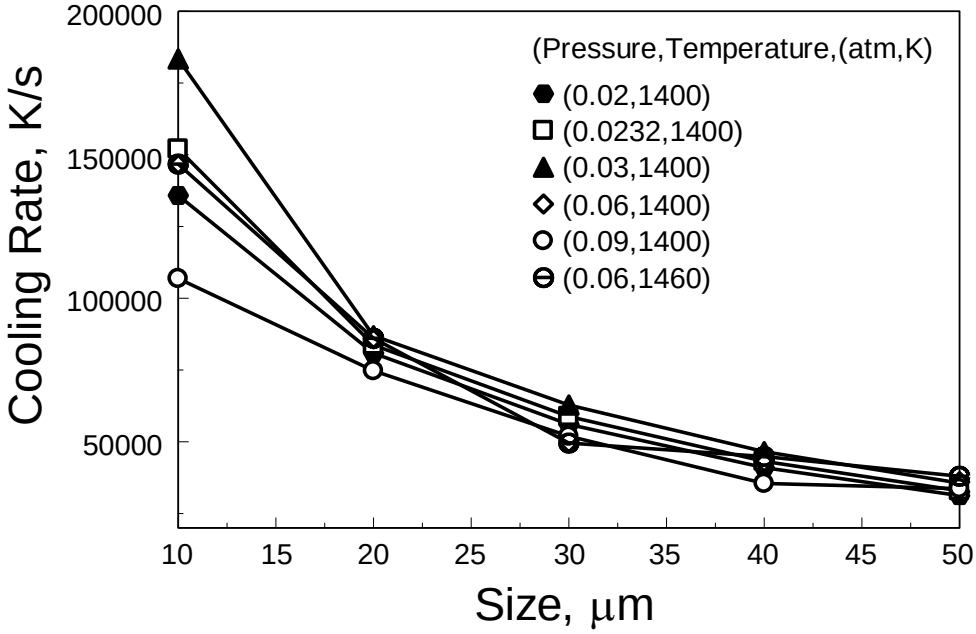

Figure 4.17 Estimated particle cooling rate as a function of particle size for various downstream pressures.

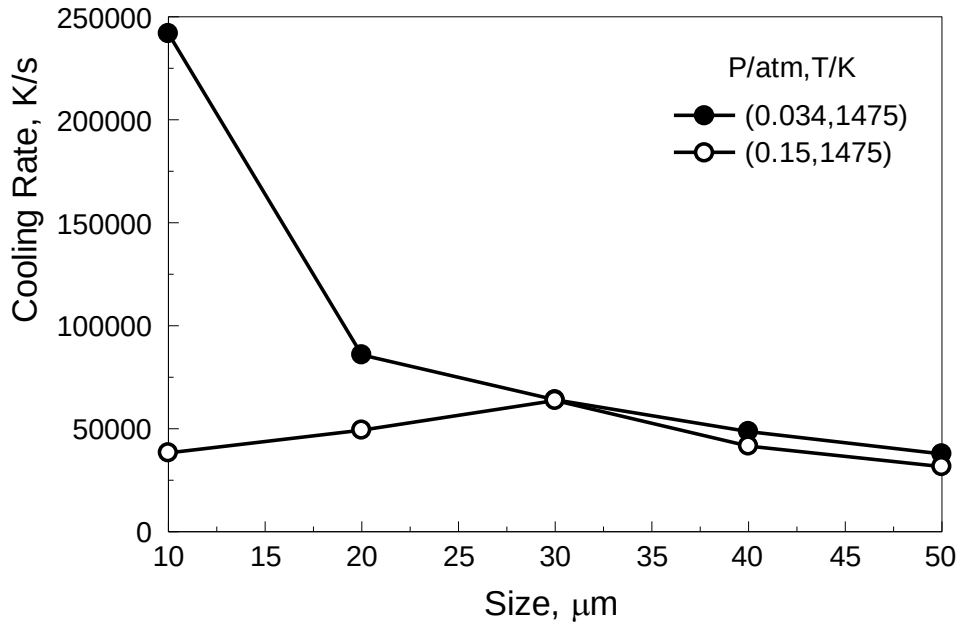

Figure 4.18 Estimated particle cooling rate as a function of particle size for various downstream pressures.

4.5 Results

4.5.1 Particle Physical Properties

SEM micrographs of the glass particles before and after exposure are shown in Figure 4.19. The fresh particles are non-spherical with sharp edges. The effect of melting is clearly observed, the recovered particles are spherical and can be easily distinguished from partially molten and non-molten material.

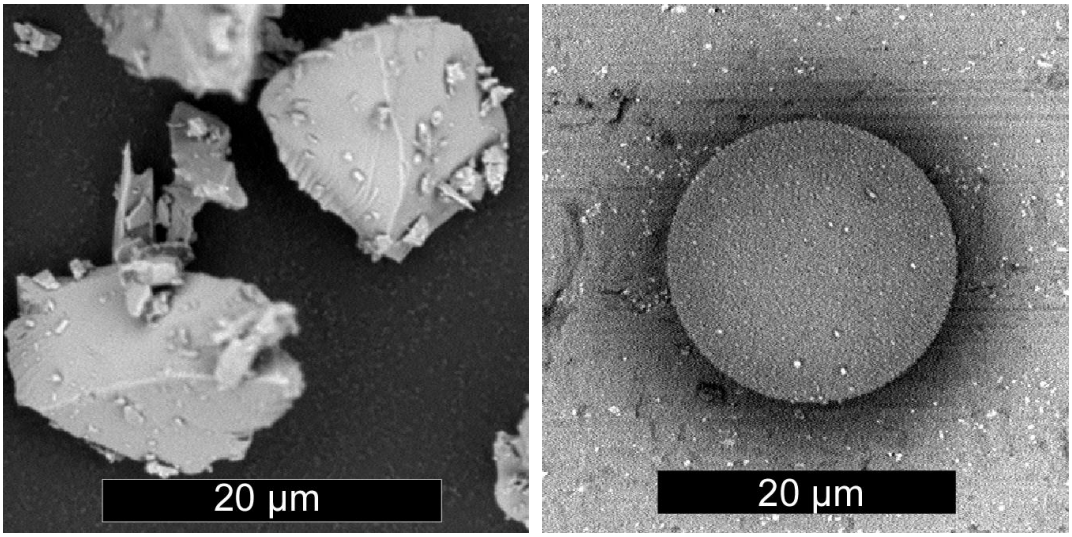

Figure 4.19 Glass particles before and after exposure.

4.5.2 Raman Indicator

A typical Raman spectrum of fresh soda lime glass is shown in Figure 4.20. The observed signal is in good agreement with literature data [50, 52, 54]. The band observed around 800 cm-1 has been attributed to Si-O stretching vibrations [49, 50]. The band observed between 850 cm-1 and 1300 cm-1 has been attributed to symmetric and asymmetric stretching of Q2, Q3, and Q4 species (SiO4 tetrahedral units with two, three and four bridging oxygen atoms, respectively) [50, 55, 56]. It was attempted to deconvolve the observed Raman patterns using OMNIC® software. The spectral region between 850 cm-

1 and 1300 cm-1 was described with five Gaussian peaks. The positions of the individual peaks were fixed while the width and intensity of the peaks were unrestricted. Due to the large overlap and poor constraints on the shapes of the component peaks, however, the results were not unique. Instead of deconvolution, the spectra were therefore processed using the basic observation that the overall maximum near 1100 cm-1 is affected by the relative abundances of Q3 vs. Q4 species, and therefore affords some sensitivity to the degree of SiO4 polymerization. The peak tips between 1050 cm-1 and 1150 cm-1 were fitted with a second order polynomial to compensate for noise, and without making any assumptions about the underlying peak shape.

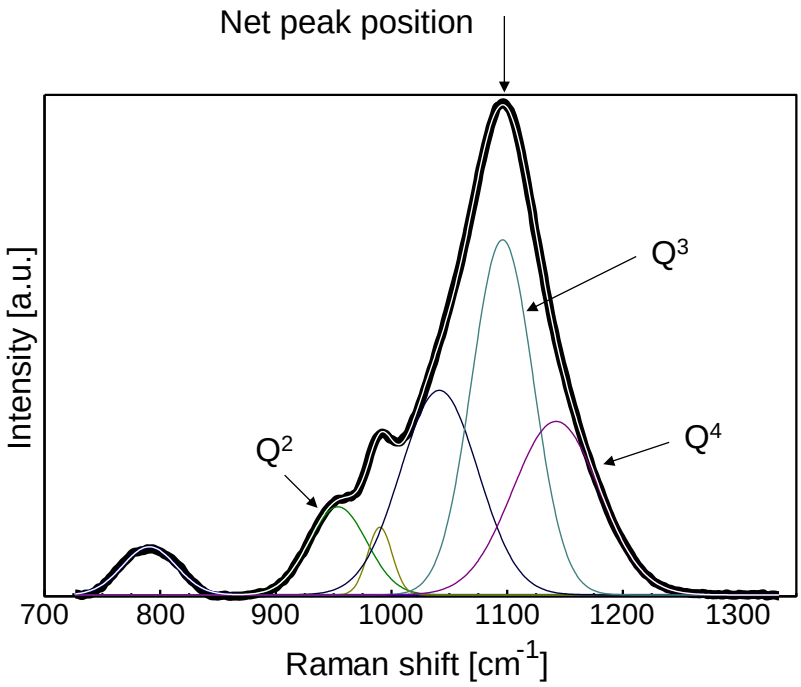

Figure 4.20 Deconvoluted Raman spectra of fresh soda lime glass particles.

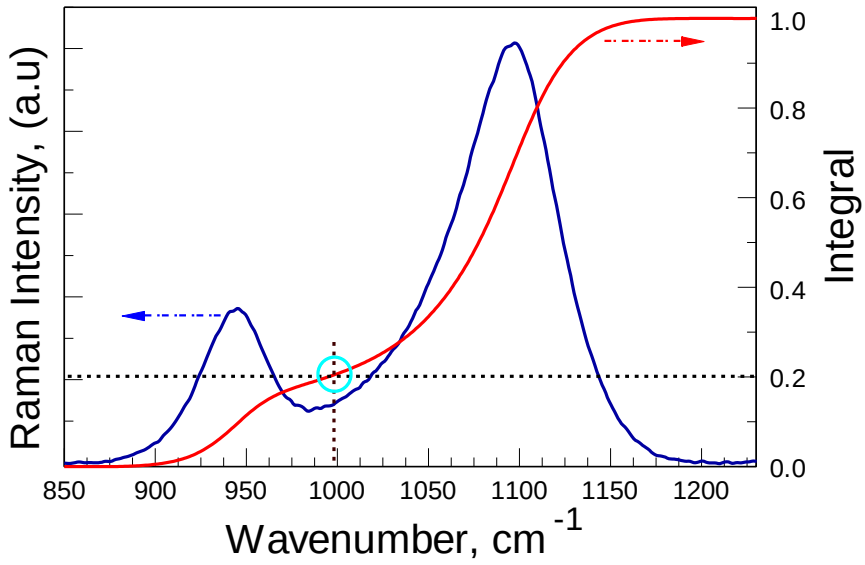

Figure 4.21 Raman spectrum and the integral of the Raman spectrum of fresh NS2 glass.

A Raman spectrum for the sodium silicate glass (NS_2) is shown in Figure 4.21. The peak positions attributable to Q_3 species showed least sensitivity to change in cooling rates. However, when integrating the Raman signal between 850 cm^{-1} and 1250 cm^{-1}, the wave number corresponding to 20% of the total integral value showed noticeable variation. The overall integral of the Raman species accounts for the summation of all the Q species present in the wavenumber window. The region between 850 cm^{-1} and ~1000 cm^{-1} is predominantly representative of the Q_2 species and the rest of the signal corresponding to Q_3 species. The amount of Q_2 vs Q_3 determines the shape of the Raman signal and hence the integral. For NS_2 glass, it was observed that the region around 20% of the integral showed the most sensitivity to variation in cooling rate.

The Raman signal for particles collected in the tube furnace experiments were also subjected to either peak position determination procedure (window glass) or peak integral procedure (NS_2 glass). The estimated cooling rates for various particle sizes obtained from Ansys simulations were combined with the Raman indicator data. The

Raman peak position variation as a function of cooling rate for both NS2 glass and window glass are shown in Figure 4.22, and Figure 4.23, respectively.

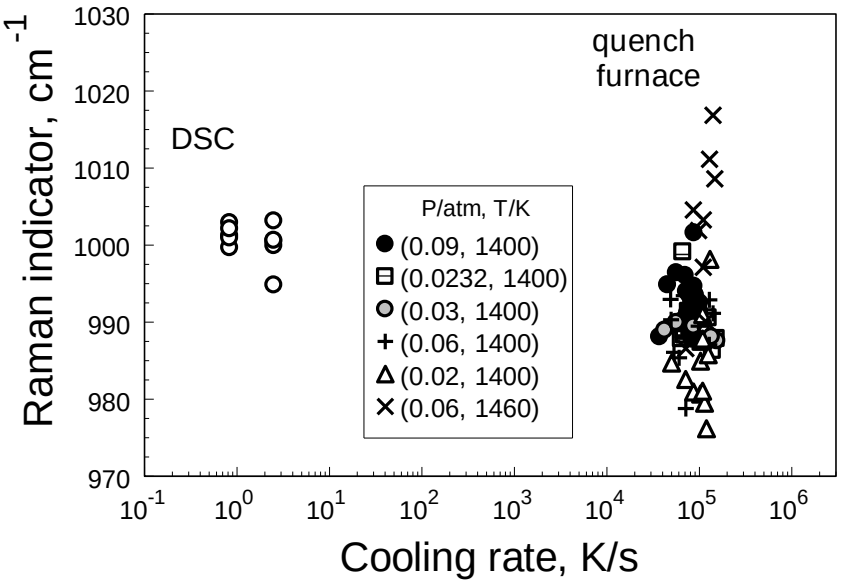

Figure 4.22 NS2 glass, Raman indicator vs cooling rate for different operating conditions.

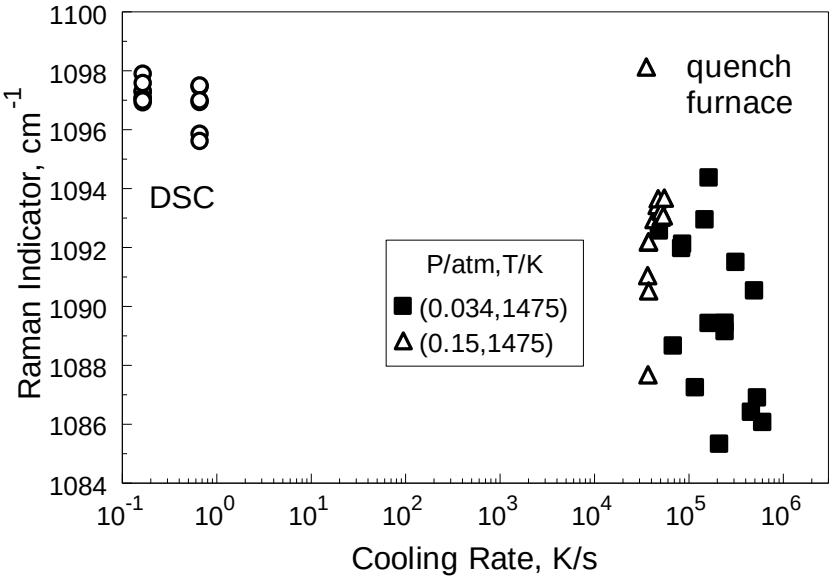

Figure 4.23 Soda lime glass, Raman indicator vs cooling rate for different operating conditions.

4.6 Discussion

Figure 4.22 shows that there is a measurable shift with cooling rate in the respective Raman indicator for rapidly quenched NS2 glass and for soda lime glass. The respective trends amount to approximately 10 wavenumbers over a 5 orders of magnitude change in the cooling rate for NS2, and 12 for soda lime glass.

While this is eminently measurable, the individual data points collected from the quench furnace show scatter that exceeds the difference to the data from the slowly cooled glass.

The numeric simulations have shown that it is unlikely that this difference reflects actual variations in cooling rate: residence times in the collection setup are generally less than 50 ms (Figure 4.15). This takes the particle from the upstream temperature (~1400 K) to room temperature. Even though the cooling profile is nonlinear as shown in Figure 4.15, the lowest cooling rate should be within an order of magnitude of ~1100 K/ 50 ms = 22,000 K/s. Therefore, upwards deviations – indicators that appear to point to cooling rates even below the DSC measurements – must reflect the inherent uncertainty or noise in the Raman measurement.

It can also not be ruled out that an error was introduced in the experiment by extended exposure of the NS2 glass particles to high temperatures in the upstream section of the furnace. No particular flow control was implemented there, allowing the particles enough time to melt. This exposure could in principle lead to partial loss of the relatively volatile sodium component [62], which would lead to increased polymerization of the SiO_2 network, and an increase in the concentration of Q_3 and Q_4 species. In both glasses this would lead to a systematic shift of the respective Raman indicator to higher values.

Since it was not feasible to measure the composition of individual particles, it is not possible to verify or quantify this effect. The observation that the experiment with NS2 glass that was conducted with a 1460 K upstream temperature shows the greatest upward scatter supports this notion, however.

For deviations towards lower Raman indicators, it is conceivable that particles experienced higher cooling rates than estimated by the simulations. Particles could quench by touching a cool section of the wall, or they could quench on the collection substrate. Considering the upward scatter, and the general particle trajectories (Figure 4.13), it is more likely, however, that this reflects the uncertainty in the Raman measurement as well.

In a revised experiment, one would operate at the lowest upstream temperature that is necessary to reliably melt the glass particles in order to minimize any compositional alteration of the particles.

More problematic than the observed scatter is the fact that in the current version of the quench setup, the downstream pressure has negligible effect on the cooling rate (Figure 4.17). Adiabatic expansion therefore does not usefully contribute to the downstream gas environment. It would be more useful to work at slightly higher pressures, which would decrease linear velocity in axial direction, and increase drag and heat transfer. Particles would follow the gas flow more closely because of the increased drag, and be cooled more effectively. The collection tube could be actively cooled, lowering the wall temperature, and therefore the internal gas temperature, and a wide variation of cooling rate with particle size could be achieved.

4.7 Conclusion

The use of glass particles as thermal witness materials was investigated. Two glasses, soda-lime glass or window glass and NS2 glass were chosen as primary sensor candidates. The variation of glass structure as a function of cooling rate was investigated by subjecting the glass is a rapid quenching experiment operated under choked flow conditions. Raman spectroscopy was used as an indicator to determine the variation of the glass structure. Two techniques i.e. peak fitting procedure (window glass - Q_3 silicon species peak position) and the signal integration method (NS2 glass – wavenumber at 20% signal integration) were employed as structural indicators.

Rapid quenching setup was modelled using Ansys Fluent. The results from the simulation indicated that for the present setup, the adiabatic expansion of gas had little impact in influencing the quenching environment. The glass particles in the experiment cooled in a similar temperature environment irrespective of the operating pressures. As a result, particles collected from this experiment experienced a narrow range of cooling rates. Raman indicator as a function of cooling rate showed significant scatter in the vertical axis. The scatter in the data could be due to poor Raman signal, uncertainty in the trajectory of the particle i.e. interaction of the particle with the wall, quenching of the particle on the collection foil, or compositional variations due to uncontrolled high-temperature exposure. When the Raman indicator is compared with the experiments performed in the DSC, the variation of the indicator over a wide range of cooling rates is small.

The results suggest that it could in principle be possible to determine particle cooling rates after recovery to within an order of magnitude. This would require a

reliability, or reproducibility of the Raman indicator of about three wavenumbers. Using Equation (4.4), this allows the recovery of a set of environment temperatures. To get the full cooling history, environment cooling rates need to be determined following the scheme outlined in section 4.2. The difference between environment cooling rate and particle cooling rate – proportional to the time derivative of the particle cooling rate may be difficult to determine. As outlined, assuming that particle cooling rate and environment cooling rate are identical leads to a quantifiable bias in the environment temperature profile, which may be acceptable depending on the application.

To obtain a better resolution, and describe the environment temperature profile with higher accuracy, glasses with higher sensitivity to structural change along with improved resolution in the analysis tool are required.

CHAPTER 5

CONCLUSION

Two types of thermosensors, each with its unique response to thermal events were investigated. Synthetic K-H_3O jarosite a synthetic analog of a common mineral, as a potential thermal witness material was explored. A complex model for the decomposition of K-H_3O jarosite was established based on thermoanalysis data up to temperatures of 1100 K. Individual decomposition steps describe the loss of $(OH)^-$ groups, SO_3, adsorbed water, and the crystallization of amorphous Fe_2O_3. Major solid intermediate products are $KFe(SO_4)_2$, yavapaiite, amorphous, β- and α-Fe_2O_3, and $K_3Fe(SO_4)_3$. Final products are α-Fe_2O_3 and K_2SO_4. The model combines sequential and parallel individual reactions and the reactions are described using constant kinetic triplets. Activation energies were estimated from isoconversion analysis and pre-exponential factors were adjusted to match the observed decomposition curves. Individual reaction models, based on the degree of conversion of the individual reactions, were left at first-order where possible. Despite these simplifications, the model well describes the present experiments and is broadly consistent with previously reported decomposition behavior of K-jarosite and H3O-jarosite.

A flow furnace experiment was designed to expose a jarosite aerosol to temperatures up to 1200 K, for times of 10 seconds and less. The jarosite particles partially decomposed during this exposure, were recovered, and the residual decomposition was determined by TG. In parallel, the partial decomposition in the flow furnace as well as the residual decomposition were calculated based on a previously

published kinetic decomposition model. Experimental and calculated residual decomposition curves are in reasonable agreement. The overall mass loss matches well. Although details of the residual decomposition curves are less reproducible and their measurement is limited by the resolution of the TG experiments, temperatures and flow rates used in the experiments are recovered well under conditions where the (OH)– groups of the jarosite are partially lost.

A sensitivity analysis of the decomposition model shows that it has the greatest power to resolve temperature and flow rate differences in the flow furnace if the temperature is near 800 K, which coincides with the loss of (OH)– groups from the jarosite structure. In this temperature region, in order to resolve a 100 K temperature difference in flow furnace conditions, the residual decomposition must be determined with a resolution better than about 1.5 wt-%. At higher temperatures, where the decomposition causes the loss of SO3 from the jarosite structure, the resolution requirement for the residual decomposition measurements is too stringent for their practical use.

The difference in sensitivity associated with the (OH)– loss vs. the SO3 loss suggests that if one were to search for suitable thermal witness materials or aim to design novel materials for this purpose, a set of parallel reactions are more useful regardless of the overall weight loss than a set of sequential reactions.

The use of glass particles as thermal witness materials was investigated. Two glasses, soda-lime glass or window glass and NS2 glass were chosen as primary sensor candidates. The variation of glass structure as a function of cooling rate was investigated by subjecting the glass is a rapid quenching experiment operated under choked flow

conditions. Raman spectroscopy was used as an indicator to determine the variation of the glass structure. Two techniques i.e. peak fitting procedure (window glass - Q3 silicon species peak position) and the signal integration method (NS2 glass – wavenumber at 20% signal integration) were employed as structural indicators.

Rapid quenching setup was modelled using Ansys Fluent. The results from the simulation indicated that for the present setup, the adiabatic expansion of gas had little impact in influencing the quenching environment. The glass particles in the experiment cooled in a similar temperature environment irrespective of the operating pressures. As a result, particles collected from this experiment experienced a narrow range of cooling rates. Raman indicator as a function of cooling rate showed significant scatter in the vertical axis. The scatter in the data could be due to poor Raman signal, uncertainty in the trajectory of the particle i.e. interaction of the particle with the wall, quenching of the particle on the collection foil, or compositional variations due to uncontrolled high-temperature exposure. When the Raman indicator is compared with the experiments performed in the DSC, the variation of the indicator over a wide range of cooling rates is small.

The results suggest that it could in principle be possible to determine particle cooling rates after recovery to within an order of magnitude. This would require a reliability, or reproducibility of the Raman indicator of about three wavenumbers. Using Equation (4.4), this allows the recovery of a set of environment temperatures. To get the full cooling history, environment cooling rates need to be determined following the scheme outlined in section 4.2. The difference between environment cooling rate and particle cooling rate – proportional to the time derivative of the particle cooling rate may

be difficult to determine. As outlined, assuming that particle cooling rate and environment cooling rate are identical leads to a quantifiable bias in the environment temperature profile, which may be acceptable depending on the application.

Application of the evaluated material to real-world combustion environments remains to be evaluated separately. For the case of K-H3O jarosite sensors, the effect of time scales, pressure and also the concentrations of certain species in the combusting environment like oxygen, SOx etc. on the decomposition kinetics. Regarding time scales, while heating rates may be much higher than used in this study, cooling rates in the absence of adiabatic expansion are relatively slow, and total exposure times can also measure in seconds. Fidelity of the temperature history may be sacrificed for an overall, integral temperature dose parameter. Regarding decomposition kinetics, while the decomposition of simpler materials are unquestioningly better characterized, it is essential to use complex materials with independent decomposition reactions in order to decouple time and temperature. As the kinetic models improve, pressure effects and also the interaction with the environment can more effectively be taken into account.

For the case of glass sensors, determination of the temperature profile during the temperature ramp in combustion events is not feasible. For combustion cases dominated predominantly by the cooling can be investigated with this type of sensors. Issues pertaining to the choice of sensors need to be resolved. Identifying glass composition with maximum sensitivity to temperature change must be performed. These sensors are desired to have wide resolvable change in their indicator (i.e. Raman signal, NMR spectrum or any other analysis tool that provides structural information) over a wide range of cooling rates. The interaction of the sensors with the particulate matter in

combustion events must be investigated prior practical application. The kinetics associated with the structural arrangement allows these sensors to resolve higher range of cooling rates; these types of sensors become more practical as the resolution offered by the analysis technique improves.

REFERENCES

1. Nelson, R.W., *Nuclear "Bunker Busters" would more likely disperse than destroy buried stockpiles of biological and chemical agents.* Science & Global Security, 2004. **12**(1-2): p. 69-89.

2. Dutrizac, J.E. and J.L. Jambor, *Jarosites and their application in hydrometallurgy.* Reviews in Mineralogy and Geochemistry, 2000. **40**(1): p. 405-452.

3. Stoffregen, R.E., C.N. Alpers, and J.L. Jambor, *Alunite-jarosite crystallography, thermodynamics, and geochronology,* 2000. p. 453-479.

4. Dutrizac, J.E. and T.T. Chen, *A mineralogical study of the jarosite phase formed during the autoclave leaching of zinc concentrate.* Canadian Metallurgical Quarterly, 1984. **23**(2): p. 147-157.

5. Klingelhöfer, G., et al., *Jarosite and hematite at meridiani planum from opportunity's Mössbauer spectrometer.* Science, 2004. **306**(5702): p. 1740-1745.

6. Madden, M.E.E., R.J. Bodnar, and J.D. Rimstidt, *Jarosite as an indicator of water-limited chemical weathering on Mars.* Nature, 2004. **431**(7010): p. 821-823.

7. Clark, B.C., et al., *Chemistry and mineralogy of outcrops at meridiani planum.* Earth and Planetary Science Letters, 2005. **240**(1): p. 73-94.

8. Frost, R.L., M.L. Weier, and W. Martens, *Thermal decomposition of jarosites of potassium, sodium and lead.* Journal of Thermal Analysis and Calorimetry, 2005. **82**(1): p. 115-118.

9. Frost, R.L., et al., *Thermal decomposition of hydronium jarosite (H3O)Fe 3(SO4)2(OH)6.* Journal of Thermal Analysis and Calorimetry, 2006. **83**(1): p. 213-218.

10. Xu, H., et al., *Thermal expansion and decomposition of jarosite: a high-temperature neutron diffraction study.* Physics and Chemistry of Minerals, 2010. **37**(2): p. 73-82.

11. Denis, G., et al., *Time-resolved measurements of optically stimulated luminescence of Al2O3:C and Al2O3:C,Mg.* Radiation Measurements, 2011. **46**(12): p. 1457-1461.

12. Gunawidjaja, R., T. Myint, and H. Eilers, *Correlation of optical properties and temperature-induced irreversible phase transitions in europium-doped yttrium*

carbonate nanoparticles. Journal of Solid State Chemistry, 2011. **184**(12): p. 3280-3288.

13. Wang, J. and L. Huang, *Thermometry based on phonon confinement effect in nanoparticles.* Applied Physics Letters, 2011. **98**(11): p. 113102-3.

14. Ruggirello, K.P., et al., *A reaction progress variable modeling approach for non-ideal multiphase explosives.* International Journal of Multiphase Flow, 2012. **42**(0): p. 128-151.

15. Drouet, C. and A. Navrotsky, *Synthesis, characterization, and thermochemistry of K-Na-H3O jarosites.* Geochimica et Cosmochimica Acta, 2003. **67**(11): p. 2063-2076.

16. Gerald, P.B., S.S. Earl, and A. Richard, *Sulfate studies II. Solid solution between alunite and jarosite.* The American Mineralogist, 1962. **47**(1): p. 112-126.

17. Gerald, P.B. and F. Michael, *Sulfate studies IV: The jarosite-natrojarosite-hydronium jarosite solid solution series* The American Mineralogist, 1965. **50**(10): p. 1595-1607.

18. Dutrizac, J.E., *Factors affecting alkali jarosite precipitation.* Metallurgical Transactions B, 1983. **14**(4): p. 531-539.

19. John W. Anthony, et al., *Elements, sulfides, sulfosalts.* Handbook of Mineralogy. Vol. 1. 1990; Tucson, Arizona, Mineralogical Society of America.

20. Larson, A.C. and R.B. Von Dreele, *General structure analysis system.* Los Alamos National Laboratory Report LAUR, 2004: p. 86-748.

21. Basciano, L.C. and R.C. Peterson, *Jarosite hydronium jarosite solid-solution series with full iron site occupancy: Mineralogy and crystal chemistry.* American Mineralogist, 2007. **92**(8-9): p. 1464-1473.

22. Majzlan, J., et al., *Thermodynamic properties, low-temperature heat-capacity anomalies, and single-crystal X-ray refinement of hydronium jarosite, (H3 O)Fe3(SO4)2(OH)6.* Physics and Chemistry of Minerals, 2004. **31**(8): p. 518-531.

23. Alonso, M., A. López-Delgado, and F.A. López, *A kinetic study of the thermal decomposition of ammoniojarosite.* Journal of Materials Science, 1998. **33**(24): p. 5821-5825.

24. Vyazovkin, S., *Modification of the integral isoconversional method to account for variation in the activation energy.* Journal of Computational Chemistry, 2001. **22**(2): p. 178-183.

25. Földvári, M., F. Paulik, and J. Paulik, *Possibility of thermal analysis of different types of bonding of water in minerals.* Journal of Thermal Analysis, 1988. **33**(1): p. 121-132.

26. Frost, R.L., et al., *A thermogravimetric study of the alunites of sodium, potassium and ammonium.* Thermochimica Acta, 2006. **443**(1): p. 56-61.

27. Starink, M.J., *The determination of activation energy from linear heating rate experiments: a comparison of the accuracy of isoconversion methods.* Thermochimica Acta, 2003. **404**(1–2): p. 163-176.

28. Vyazovkin, S., et al., *ICTAC Kinetics Committee recommendations for performing kinetic computations on thermal analysis data.* Thermochimica Acta, 2011. **520**(1-2): p. 1-19.

29. Gordon, J.M., K.C. Gross, and G.P. Perram, *Temporally resolved infrared spectra from the detonation of advanced munitions.* Sensors and Systems for Space Applications III, 2009. **7330**.

30. Feng, X.J., et al., *Effect of aluminium content on the detonation pressure and shock wave parameters of TNT/Al explosives.* Huozhayao Xuebao/Chinese Journal of Explosives and Propellants, 2009. **32**(5): p. 1-4.

31. Feng, X.J., et al., *Effect of AP on the air explosion parameters of explosive.* Huozhayao Xuebao/Chinese Journal of Explosives and Propellants, 2010. **33**(2): p. 40 - 44.

32. Peuker, J.M., et al., *Optical depth measurements of fireballs from aluminized high explosives.* Optics and Lasers in Engineering, 2009. **47**(9): p. 1009-1015.

33. Eilers, H., et al. *Irreversible phase transitions in doped metal oxides for use as temperature sensors in explosions*. AIP Conference Proceedings, 2012. **1426**, p. 1577-1580.

34. Wang, J. and L. Huang, *Thermometry based on phonon confinement effect in nanoparticles.* Applied Physics Letters, 2011. **98**(11), p. 113102.

35. Su, J., et al., *Ga filled nanothermometers with high sensitivity and wide measuring range.* Journal of Nanoscience and Nanotechnology, 2012. **12**(8): p. 6397-6400.

36. Drouet, C. and A. Navrotsky, *Synthesis, characterization, and thermochemistry of K-Na-H 3O jarosites.* Geochimica et Cosmochimica Acta, 2003. **67**(11): p. 2063-2076.

37. Purtyman, W.D. *Chemical quality of surface water in bandelier national monument*. Los Alamos, New Mexico, 1984.

38. Mohan, S., M.A. Trunov, and E.L. Dreizin, *Heating and ignition of metal particles in the transition heat transfer regime.* Journal of Heat Transfer, 2008. **130**(10).

39. Incropera, F.P. and D.P. DeWitt, *Fundamentals of heat and mass transfer, 4th Edition*. 1996, New York, New York: John Wiley & Sons.

40. Touloukian, Y.S., *Thermophysical Properties of Matter: Thermal conductivity : nonmetallic solids*. 1970, New York, New York: IFI/Plenum.

41. Akiyama, T., et al., *Measurement and modeling of thermal conductivity for dense iron oxide and porous iron ore agglomerates in stepwise reduction.* ISIJ International, 1992. **32**(7): p. 829-837.

42. Suleiman, B.M., et al., *Thermal properties of lithium sulphate.* Journal of Physics D: Applied Physics, 1997. **30**(18): p. 2553-2560.

43. Badgujar, D.M., et al., *Advances in science and technology of modern energetic materials: An overview*. Journal of Hazardous Materials, 2008. **151**(2–3): p. 289-305.

44. Agrawal, J.P., *Salient features of explosives*, in *high energy materials*. 2010, .New York, New York ,Wiley-VCH Verlag GmbH & Co. KGaA.

45. Boddington, T., et al., *Kinetic analysis of temperature profiles of pyrotechnic systems.* Combustion and Flame, 1986. **63**(3): p. 359-368.

46. Hertzberg, M., I.A. Zlochower, and K.L. Cashdollar, *Metal dust combustion: explosion limits, pressures, and temperatures.* Symposium (International) on Combustion, 1992. **24**(1): p. 1827-1835.

47. Li, Z.Y., et al., *Study on flame temperature measurement of pyrotechnics using multi-spectral thermometer.* Guang Pu Xue Yu Guang Pu Fen Xi/Spectroscopy and Spectral Analysis, 2010. **30**(8): p. 2062-2064.

48. Weiser, V. and N. Eisenreich, *Fast emission spectroscopy for a better understanding of pyrotechnic combustion behavior.* Propellants, Explosives, Pyrotechnics, 2005. **30**(1): p. 67-78.

49. Hannon, A.C., B. Vessal, and J.M. Parker, *The structure of alkali silicate glasses.* Journal of Non-Crystalline Solids, 1992. **150**(1-3): p. 97-102.

50. McMillan, P. and B. Piriou, *Raman spectroscopic studies of silicate and related glass structure: a review.* Bulletin de Mineralogie, 1983. **106**(1-2): p. 57-75.

51. Halter, W.E. and B.O. Mysen, *Melt speciation in the system Na2O-SiO2.* Chemical Geology, 2004. **213**(1-3): p. 115-123.

52. Mysen, B.O., D. Virgo, and C.M. Scarfe, *Relations between the anionic structure and viscosity of silicate melts - A Raman spectroscopic study.* Am. Mineral., 1980. **65**: p. 690-710.

53. Richet, P., et al., *Configurational heat capacity and entropy of borosilicate melts.* Journal of Non-Crystalline Solids, 1997. **211**(3): p. 271-280.

54. Colomban, P., et al., *Raman identification of ancient stained glasses and their degree of deterioration.* Journal of Raman Spectroscopy, 2006. **37**(5): p. 614-626.

55. Deschamps, T., et al., *Soda-lime silicate glass under hydrostatic pressure and indentation: A micro-Raman study.* Journal of Physics Condensed Matter, 2011. **23**(3).

56. McMillan, P.F., et al., *A study of SiO2 glass and supercooled liquid to 1950 K via high-temperature Raman spectroscopy.* Geochimica et Cosmochimica Acta, 1994. **58**(17): p. 3653-3664.

57. Angeli, F., et al., *Effect of temperature and thermal history on borosilicate glass structure.* Physical Review B - Condensed Matter and Materials Physics, 2012. **85**(5).

58. Möncke, D., et al., *Thermal history of a low alkali borosilicate glass probed by infrared and Raman spectroscopy.* Glass Technology: European Journal of Glass Science and Technology Part A, 2006. **47**(5): p. 133-137.

59. Moynihan, C.T., A.J. Easteal, and M.A. DeBolt, *Dependense of the fictive temperature of glass on cooling rate.* Journal of the American Ceramic Society, 1976. **59**(1-2): p. 12-16.

60. ANSYS, Fluent User Guide Manual. http://cdlab2.fluid.tuwien.ac.at/LEHRE/TURB/Fluent.Inc/v140/flu_ug.pdf (accessed on July 3rd 2014).

61. webbook.nist.gov/cgi/cbook.cgi?ID=C1302938&Type=JANAFS&Table=on. (accessed on July 3rd 2014)

62. Van Limpt, H., Beerkens, R., Verheijen, O., *Models and experiments for sodium evaporation from sodium containing silicate melts*. Journal of the American Ceramic Society, 2006. **89** (11), p. 3446-3455.